

**3-DIMENSIONAL ELECTRON MICROSCOPY OF BIOLOGICAL SPECIMENS**

by

Korrinn M. Strunk

BS, Carnegie Mellon University, 2009

Submitted to the Graduate Faculty of  
The Swanson School of Engineering in partial fulfillment  
of the requirements for the degree of  
Master of Science

University of Pittsburgh

2012

UNIVERSITY OF PITTSBURGH  
SWANSON SCHOOL OF ENGINEERING

This thesis was presented

by

Korrinn M. Strunk

It was defended on

March 23, 2012

and approved by

John A. Barnard, PhD, Professor, Department of Mechanical Engineering and Materials Science

Jörg M.K. Wiezorek, PhD, Associate Professor, Department of Mechanical Engineering and

Materials Science

Thesis Advisor: Jennifer L. Gray, PhD, Assistant Professor, Department of Mechanical

Engineering and Materials Science

Copyright © by Korrinn Strunk

2012

## **3D ELECTRON MICROSCOPY OF BIOLOGICAL SPECIMENS**

Korrinn M. Strunk, MS

University of Pittsburgh, 2012

Three-dimensional (3D) imaging is an important tool in electron microscopy, especially in biological specimens where the main focus is the structure of the cells. Many times important information is lost because the exact orientation of a specimen is unknown. We tested two different 3D imaging techniques, focused ion beam (FIB) slice and view, and cryo-FIB thinning of samples for use in cryo transmission electron tomography (cryo-TEM) and cryo-electron tomography (cryo-ET).

We began our research with room temperature FIB slice and view, with an intention to move onto slice and view at cryogenic temperatures. We found this technique to be difficult to control and the time required to produce results was simply too high. We moved on to investigating cryo-FIB milling as a tool for thinning cryo-ET specimens. Advances in cryo-ET have enabled high-resolution 3D imaging of complex assemblies and determination of cellular architectures in their close-to-native states. However, one major limitation, the accessible specimen thickness, has hindered its broader application in cellular biology. Recent efforts have been made to create thin, frozen-hydrated sections using cryo-ultramicrotomy, but with many mechanical artifacts and low yields. Here, we report a method that applies a focused ion beam (FIB) at cryogenic temperature (cryo-FIB) to reduce the thickness of frozen-hydrated cells, including mammalian cells, to a degree suitable for cryo-ET.

## TABLE OF CONTENTS

<b>PREFACE.....</b>	<b>IX</b>
<b>1.0 INTRODUCTION.....</b>	<b>1</b>
<b>2.0 BACKGROUND INFORMATION .....</b>	<b>4</b>
<b>2.1 CRYO-TEM.....</b>	<b>4</b>
<b>2.2 TOMOGRAPHY .....</b>	<b>8</b>
<b>2.2.1 Overview .....</b>	<b>8</b>
<b>2.2.2 Cryo-ET .....</b>	<b>12</b>
<b>2.3 THINNING BIOLOGICAL SPECIMENS.....</b>	<b>13</b>
<b>2.3.1 Previous Techniques .....</b>	<b>13</b>
<b>2.4 CURRENT STATE OF THE ART .....</b>	<b>15</b>
<b>2.4.1 FIB Slice-and-View .....</b>	<b>15</b>
<b>2.4.2 Cryo-FIB Milling.....</b>	<b>20</b>
<b>3.0 EXPERIMENTAL METHODS .....</b>	<b>22</b>
<b>3.1 FIB SLICE AND VIEW.....</b>	<b>22</b>
<b>3.1.1 Cell preparation for FIB slice and view .....</b>	<b>22</b>
<b>3.1.2 FIB slice and view milling .....</b>	<b>23</b>
<b>3.2 CRYO-EM.....</b>	<b>24</b>
<b>3.2.1 Cell preparation for cryo-FIB/TEM .....</b>	<b>24</b>

3.2.2	Cryo-FIB Milling.....	26
3.2.3	Cryo-TEM and Cryo-ET.....	31
3.2.4	Tomogram Reconstruction.....	32
<b>4.0</b>	<b>RESULTS AND DISCUSSION .....</b>	<b>34</b>
4.1	FIB SLICE AND VIEW.....	34
4.1.1	Milling Results.....	34
4.1.2	Discussion.....	39
4.2	CRYO-EM.....	41
4.2.1	Design and Construction of the Cryo-FIB shuttle .....	41
4.2.2	Ice Quality.....	43
4.2.2.1	Granular Ice .....	43
4.2.2.2	Devitrified Ice.....	44
4.2.2.3	Directional Ice .....	45
4.2.2.4	Good Ice.....	46
4.2.2.5	Milling Artifacts.....	47
4.2.3	E. Coli.....	48
4.2.4	HeLa .....	52
<b>5.0</b>	<b>CONCLUSIONS .....</b>	<b>58</b>
5.1	FIB SLICE AND VIEW.....	58
5.2	CRYO-FIB MILLING .....	58
<b>6.0</b>	<b>FUTURE WORK.....</b>	<b>60</b>
6.1	MATERIALS SCIENCE APPLICATIONS.....	62
	<b>REFERENCES.....</b>	<b>63</b>

## LIST OF FIGURES

Figure 1: Schematic of the plunge freezing apparatus.....	6
Figure 2: Bubbling in vitrified water. ....	7
Figure 3: Soya bean phospholipd vesicles .....	8
Figure 4: Schematic drawing of an image of catalyst particles on a zeolite substrate as seen in the TEM .....	10
Figure 5: Electron tomography. ....	11
Figure 6: Progressive reduction of crevasse formation with reduction in section thickness. ....	15
Figure 7: Schematic depicting the principle of FIB milling .....	16
Figure 8: 2D and 3D imaging of yeast cells by scanning electron microscopy.....	17
Figure 9: Scanning electron microscope images of yeast cells plunge-frozen. ....	19
Figure 10: Illustration of possible FIB-milling strategies.....	21
Figure 11: FIB slice and view .....	24
Figure 12: Cryo-FIB loading and milling equipment .....	27
Figure 13: Cryo-FIB milling shuttle. ....	27
Figure 14: Milling equipment and milling orientations .....	28
Figure 15: Cryo-FIB sample and milling schematic.....	30
Figure 16: FEI Polara TEM .....	32
Figure 17: FIB slice and view overview .....	34

Figure 18: 5-minute slice and view sample .....	36
Figure 19: 25-minute slice and view sample .....	38
Figure 20: Autocad drawing of the cryo-FIB shuttle.....	42
Figure 21: Granular ice .....	44
Figure 22: Devitrified ice.....	45
Figure 23: Directional ice .....	46
Figure 24: Good ice .....	47
Figure 25: Milling artifacts .....	48
Figure 26: Cryo FIB milling of E. Coli samples.....	50
Figure 27: Tomographic reconstruction of a FIB-milled E. coli cell .....	52
Figure 28: HeLa cell milling .....	54
Figure 29: Tomographic reconstruction of a FIB-milled HeLa cell.....	55
Figure 30: Comparison of E. coli and HeLa cell grid squares.....	56
Figure 31: Overview DIC images of HeLa cells cultured on a Quantifoil gold index grid.....	57
Figure 32: Schematics of two FIB-milling strategies for producing vitrified cell lamella without “lift-out” .....	61

## **PREFACE**

The author would like to thank the members of Dr. Peijun Zhang's research group, Drs. Sangmi Jun, Gongpu Zhao, Xin Meng and Danxia Ke for their help with specimen creation, cryo-microscopy and tomography. The author would also like to thank the members of Dr. Gray's research group, Hao Wang, Gautam Reddy and Jinshi Wang for their help with FIB milling and TEM. The author would also like to thank Travis Wheeler in the University of Pittsburgh, School of Medicine Machine Shop for making the shuttle and cartridges used for FIB milling and cryo-TEM. The author would also like to thank Trevor Clark from the Pennsylvania State University for help and use of their cryo-FIB. Lastly, the author would like to thank her friends and family for all of their support and Dr. Jennifer Gray for being her adviser.

## 1.0 INTRODUCTION

Cryo-EM is important in the study of biological specimens. First developed by Fernandez-Moran in 1960 [1] and perfected by Dubochet in 1982 [2], [3], it allows for insight into the exact structure of biological specimens without altering their native states. 3D electron microscopy can be used to reconstruct the entire cell structure and provide insight into the exact position and structure of many important components of the cellular make up. A dual beam FIB/SEM can be used to create a 3D reconstruction of a bulk specimen both at room temperature [4–6], and at cryogenic temperatures [7], [8]. By using a slice and view technique, the specimens can then be reconstructed using a computer program.

Cryo-electron tomography (cryo-ET) has become an increasingly powerful method for three-dimensional (3D) structural determination of “one-of-a-kind” objects, such as whole cells, sub-cellular organelles, and macromolecular assemblies, that are preserved in the frozen-hydrated state [9–11]. It has provided a wealth of ultrastructural information of cellular compartments in bacterial cells and eukaryotic cells [12–16] and potentially allows visualization of the molecular and supramolecular architecture of cells and tissues in a close-to-native state [17], [18]. However, due to the requirement for thin specimen preparation ( $< 0.5 - 1 \mu\text{m}$ ) for transmission electron microscopy (TEM), cryo-ET structural analysis has been confined to isolated viruses [19–22], small bacterial cells [10], [14], [23–25], and very thin peripheral regions (the leading edge) or appendages of eukaryotic cells [12], [25], where useful information

can be recovered from cellular tomograms. To image and access interior structures of larger cells, in particular, mammalian cells (>5  $\mu\text{m}$ ), and high-pressure frozen tissues, a method to thin frozen-hydrated specimens to a thickness less than half a micron is necessary.

The goal of this research was to find a viable technique to apply to 3D cryo-EM, so that we can view cells in their native state. Then we can view the structures of the cells and analyze the structure. We began our research into 3D EM by using a room temperature slice and view technique on *E. coli* cells embedded in plastic resin. This technique did not yield ideal results so we focused our research on other techniques that could be viable to 3D cryo-EM.

We then moved on to techniques that can be used to mill large mammalian cells for viewing in the TEM, as well as cryo-tomography without the numerous artifacts present in vitreous sectioning. The samples must be thin enough to be electron transparent, with as few defects as possible, while keeping the cells in as close a state as possible to their native state. This was achieved using a dual beam cryo-FIB for milling and a cryo-TEM. Starting with *E. coli* cells to test our techniques and equipment, we were able to fine-tune a method that is used to mill vitreous samples. After perfecting our technique and equipment, we then moved on to milling larger HeLa cells. The milling of the larger cells required a slightly different approach because they are much larger and harder to distinguish on the TEM grids in the FIB. Using a longer milling time and higher milling current, we were able to get good results from the HeLa cell samples and tomographic reconstructions.

This paper will show the experimental techniques and tools developed to successfully mill large vitreous samples using the FIB and then perform tomography. We have successfully milled samples containing HeLa cells and have gotten very good tomography results. This

technique can be applied to other large mammalian cells and possibly to the interaction between mammalian cells and other cells, like viruses or bacteria.

## **2.0 BACKGROUND INFORMATION**

### **2.1 CRYO-TEM**

Imaging biological cells using an electron microscope has proven to be very difficult in the past. Electron microscopes operate under high vacuum and water evaporates at such low pressures. In addition, biological specimens are mostly made of carbon and are therefore very susceptible to beam damage. In the past, different methods were used to try to combat this beam damage. One method used involves the staining of the biological material before embedding in a plastic resin. While this method creates samples with high contrast and good image qualities, the dyes and plastics used alters the cells from their native states [26]. Another method involves imaging wet cells in a differentially pumped hydration chamber. However, in this method, there is a very high occurrence of beam damage and the samples cannot be exposed to the electron beam for long periods of time. Also, the scattering of water layers and drops is strong and has a pronounced effect on the resolution and contrast of the resulting images [27], [28].

The use of freezing at very low temperatures was first developed by Fernandez-Moran in 1960. The rapid freezing of tissue and biological cells suspends all physiological activity by immobilizing and preserving tissue constituents. Freezing the specimens also reduces the complex preparation artifacts present in staining and fixing that limit investigations of the native state. Close approximation of the living state requires more than the preservation of the chief

organic and inorganic constituents of the cellular organization in tissues, the most predominant of which is water [29]. By freezing the cells in their hydrated state, it is possible to preserve the water in the cells and tissues. Fernandez-Moran used liquid helium to quickly freeze tissue specimens for electron microscopy. In these samples, the ice crystals were still visible and limited the resolution of the images [1].

When water freezes, it creates small ice crystals. These crystals are larger than some of the structural features of biological samples, which cause structural damage upon freezing. It was found in the 1980's that it is possible to cool water into a vitreous (or glass-like) solid [3]. In the previous attempts to form vitreous water, the biggest obstacle was the thickness of the water layer. Fortunately, the thickness required to form vitreous water is the same thickness needed for electron microscopy ( $<0.5\mu\text{m}$ - $1\mu\text{m}$ ). The problem of how to form a sufficiently thin, stable layer of suspension was solved by Dubochet in 1984 by spanning the unsupported liquid over hole in an electron microscopy grid [30]. It was found that this vitrification of water occurs at  $-160\text{ C}$ , so conventional liquid nitrogen can be used.

The technique used for creating cryo-TEM grids involves suspending an uncoated electron microscopy grid vertically in forceps above a pot of liquid ethane cooled in liquid nitrogen. A drop of suspension containing the specimen is then applied to the grid. Most of the liquid on the grid is removed by blotting with filter paper for a few seconds and since the thin liquid layer is self-stabilizing, this method is not critical. The sample is then plunged into the liquid ethane where it vitrifies quickly (figure 1). The sample is then transferred to liquid nitrogen and mounted onto a cryo holder for use in the TEM. During imaging, a large defocus value is used to make sure of the large phase contrast [2]. There is still damage if the sample is

exposed to the beam for too long, or at too high of a dose (figure 2), so a low dose electron beam is used [3].

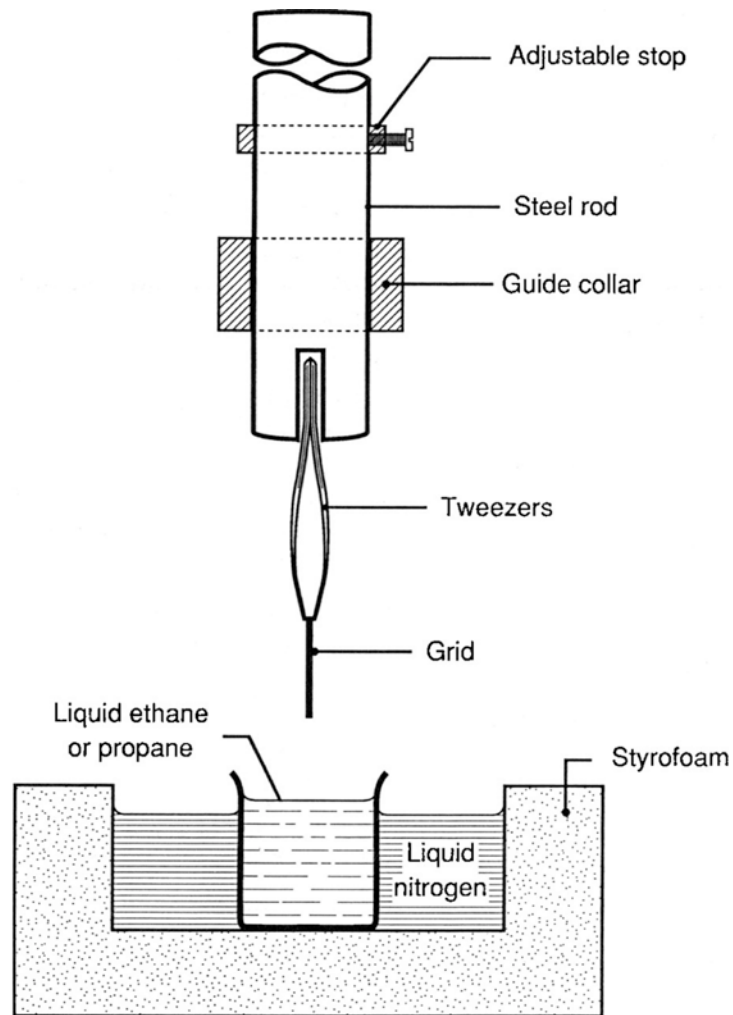


**Figure 1: Schematic of the plunge freezing apparatus [31]**

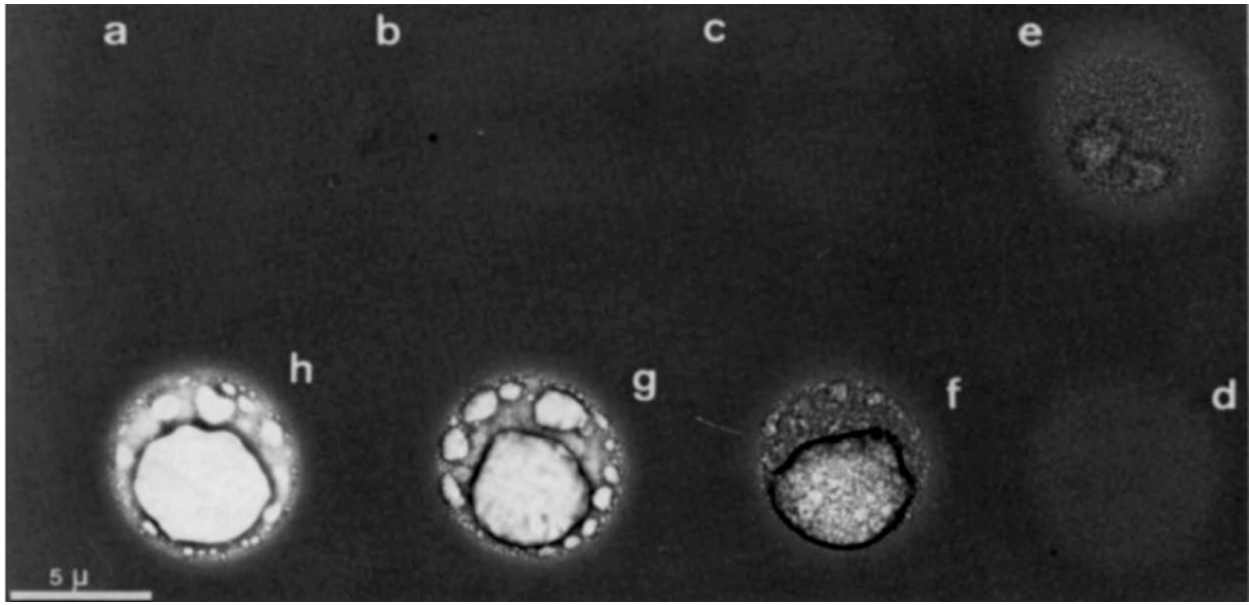


**Figure 2: Bubbling in vitrified water.** A specimen of  $0.160 \text{ g m}^{-2}$  vitreous water obtained by condensation of low pressure vapor on a cold carbon coated formvar film is irradiated at 110K in the areas a-h by electron doses of 5, 20, 40, 80, 120, 240, 340 and 450  $\text{ke nm}^{-2}$  respectively, applied at the rate of  $2 \text{ ke nm}^{-2}\text{s}^{-1}$  with 80 kV electrons [3].

Thus, it is possible to image specimens in their completely native states. A comparison in figure 3 shows the difference between vesicles in vitreous ice (figure 3 (a)) and those imaged using a staining and embedding technique (figure 3 (b)). It is possible to get a good high-resolution image using vitrification due to the signal to noise ratio. The signal from unstained, unsupported, hydrated objects is low, but not negligible. This signal difference comes from the difference in mass density between the biological material (about  $1.35 \text{ g cm}^{-3}$  for compact protein) and the vitrified medium (about  $0.93 \text{ g cm}^{-3}$  for vitrified water). This difference is substantial and allows for use of phase contrast. The noise in the image is also low because there are no contributions from stain and supporting film and the sample is not damaged during preparation [3].

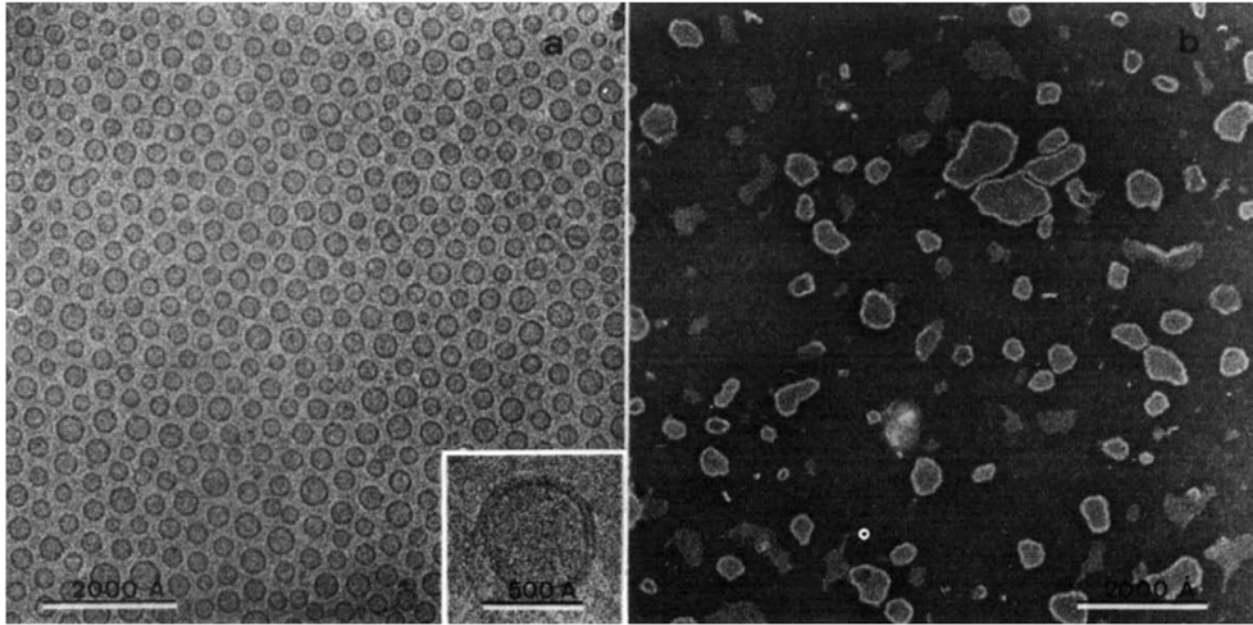


**Figure 3: Soya bean phospholipid vesicles obtained by dialysis of the lipids (1 mg ml<sup>-1</sup>) solubilized in 1% neutral detergent. (a) Thin film vitrification: thin layer of unstained, unsupported vitrified solution. Insert: enlarged view of a vesicle from another preparation. (b) Conventional preparation, negatively stained with 2% sodium phosphotungstate pH 7.2 [2].**

## 2.2 TOMOGRAPHY

### 2.2.1 Overview

DeRosier and Klug first developed the principles and methods for tomography in 1968, however the technique did not see widespread use until the 1980s when technology became more advanced [32]. The invention of computer control, improved specimen stages, highly sensitive digital image recording, field emission electron sources, and energy filtering, combined with advanced computer processing allowed the technique of electron tomography to become more refined and readily available [33].

Regular TEM images provide the user with an "xray" view of the specimen. Although this can allow the viewer to see the inside structure of the specimen, this also has a disadvantage in that structural details from different depths in the specimen are superimposed in a two dimensional projection [33]. Figure 4 shows an example of this discrepancy; in this set of images, it is not possible to discern where the particles are located when looking at the 2D projection [34]. When compared to other three dimensional microscopy techniques such as scanning confocal fluorescence and deconvolution light microscopy, electron tomography offers an improvement in resolution of 40-100 fold [35]. Tomography also occupies a place in 3D biological electron microscopy between work being done at near atomic resolution on isolated macromolecules or two dimensional protein arrays and traditional serial section reconstructions of whole cells and tissue specimens. In the field of electron microscopy, electron tomography can complement serial sectioning by providing a higher resolution in the depth dimension [33].

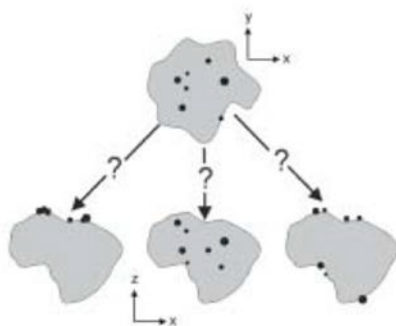


**Figure 4: Schematic drawing of an image of catalyst particles on a zeolite substrate as seen in the TEM (seen from top in x-y projection, at top) and three possible x-z configurations (seen from the side in x-z projection). Without three-dimensional information we do not know which of the three possibilities would be correct and no conclusions can be made about inter-particle distances and location on the zeolite (inside, one surface, all surfaces) [34].**

In electron tomography, the initial data is collected by tilting the specimen in the electron beam. The resolution and quality of the reconstruction are directly dependent on how finely spaced the tilt images are and over how wide an angular range they extend. Generally, this consists of collecting images at 1-2° angular interval over an angular range of  $\pm 60-70^\circ$  (figure 5 (a)). The tomographic image is then generated in a computer by back projecting each two dimensional image with appropriate weighting (figure 5 (b and c)) [35]. This is possible because the Fourier transform of a two dimensional projection of a three dimensional object is identical

to the corresponding central section of the three-dimensional transform of the object. This means that the three-dimensional transform can therefore be built up plane by plane using transforms of different projected view of the object. If sufficient data are available, the object can then be reconstructed by Fourier inversion of the resulting three-dimensional transform [32], [36].

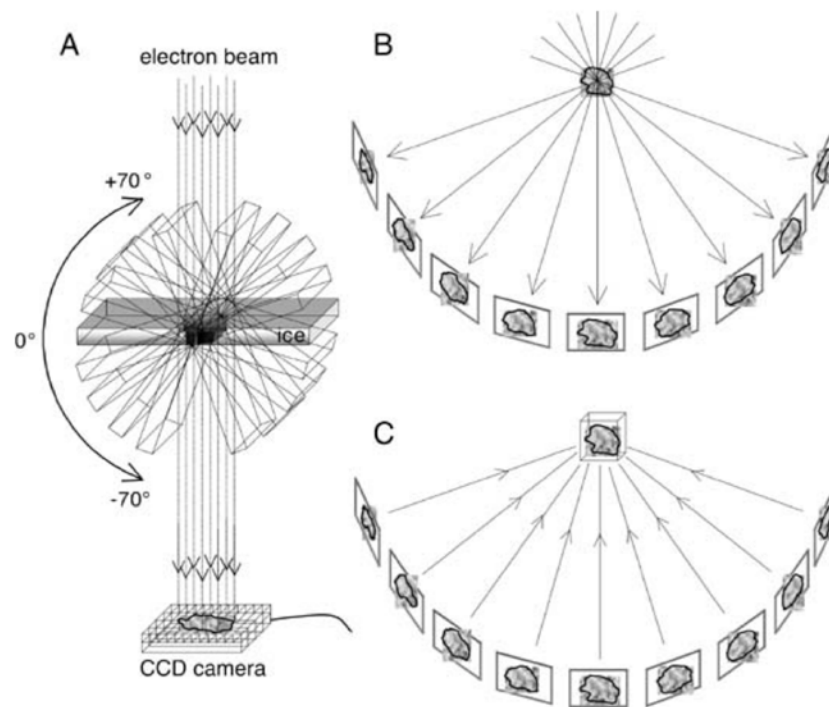


**Figure 5: Electron tomography. Two-dimensional transmission electron micrographs (projection images) are recorded at different tilt angles for individual 3D objects. (A) The specimen holder is tilted incrementally around an axis perpendicular to the electron beam, and projection images of the same specimen area (field of view) are recorded on a CCD camera at each position. Tilt increments are typically  $0.5^\circ$  to  $5^\circ$  and the tilt range is about  $\pm 70^\circ$ . A more schematic diagram (B) illustrates the images projected by a specimen at successive tilt angles. After translationally and rotationally aligning all of these projection images, the imaged object is (C) reconstructed into a 3D density map (often called the tomogram) by a weighted-backprojection procedure [37].**

The tomogram is then represented by a three dimensional block of data that is represented as an array of volume elements or voxels. These voxels are usually cubes 1-4 nm per side. Each voxel has a grayscale value that corresponds to the mass density in that region of the specimen. Since macromolecules are slightly denser than their aqueous solvent, they interact more strongly than their background with electrons in the beam of the microscope due to electron scattering. The resulting reconstruction can then be viewed in planes displayed as two-dimensional images at selected values of the third dimension. Each image displays only one slice from the main that comprises the reconstruction. The structure and position of complex features can be determined by examining neighboring slices. In biological samples, representing them with graphic models can facilitate the visualizing of complex structures. If the contrast in the resulting tomogram is good and the background is sparse, boundaries around features of interest can be identified automatically by choosing appropriate threshold values in the distribution of the three dimensional density [35].

### **2.2.2 Cryo-ET**

The methods of tomography can successfully be applied to cryogenically frozen samples. However, there are a few problems when translating traditional tomography to cryogenically frozen samples. The first problem is that the resulting images are very low contrast. This is due to the small differences in mass density between clusters of macromolecules and the frozen cytosol that surrounds them. It becomes hard to visualize the detail of cellular substructure. The objective lens in the TEM can be underfocused in order to produce of a kind of phase contrast that makes the cellular structures more distinguished from the rest of the cells [35]. A second

difficulty when performing cryo-ET is sensitivity of the sample to the electron beam. In tomography, it is important to obtain as many images as possible from as many angles as possible in order to produce the highest quality reconstruction. The problem is, with each image there is an increase in electron dose, which can cause the ice in the sample to melt, and disrupt the image [17]. In order to overcome this, the smallest dose is used, which leads to an increase in noise found in the resulting images. Due to the noise and low contrast, the resolution of cryo-ET images is currently in the region of 5-8 nm [35].

Another limitation in Cryo-ET is sample thickness. Currently, samples must be less than 0.5-1  $\mu\text{m}$ . If the thickness of the sample exceeds the mean free path of electrons, multiple inelastic scattering events begin to degrade the quality of the images, despite the use of higher voltage (300-400 keV) [12]. Thus far, cryo-ET has been confined to isolated viruses [19–22], small bacterial cells [10], [14], [23–25] and the very thin leading edge or appendages of eukaryotic cells [14], [25].

## **2.3 THINNING BIOLOGICAL SPECIMENS**

### **2.3.1 Previous Techniques**

Previous techniques have been used to thin samples for use in the TEM. The first technique used was to fix the sample chemically and then thinly slice the sample until it was electron transparent [33], [38]. As stated above, this takes the sample out of its native state and is not an ideal method for Cryo-EM and subsequent structural analysis [26]. The second most prevalent technique is

vitreous sectioning. This technique uses frozen hydrated specimens, which cannot be viewed in the TEM when they are plunge frozen.

In vitreous sectioning, the TEM specimen is cut from a vitrified specimen at -160 C and picked up dry from the knife-edge and examined in the TEM. The samples usually have a thickness of 160-200 nm [39–43]. When using this technique, in the cytoplasm the ribosome are less well defined than in published images of frozen hydrated thin sections [42].

Vitreous sectioning can also lead to many defects in the specimen. There are knife marks that are parallel to the cutting direction. Knife marks are not always visible in the projection image however they can be seen in the tomography slices. The depth of these defects is related to the size of the defects on the knife and can also be caused by build-up on the knife during cutting (figure 6, black arrows) [14]. Compression, or a shortening of the dimension of the section parallel to the cutting direction with a corresponding increase in section thickness is also another very prominent problem. Compression was found to typically be between 30 and 60% and the thickness increase is between 1.4 and 2.5 fold (figure 6) [14]. The last type of defects associated with vitreous sectioning is crevasses. This defect is unique to frozen hydrated section and is 20 to 30 nm wide elongated fissures perpendicular to the cutting direction (figure 6, white arrows). Crevasses are only observed if sections are over 100 nm in thickness or if some crystalline ice is present. The precise mechanism of formation is unknown and there is disagreement as to the cause [14], [42], [43].

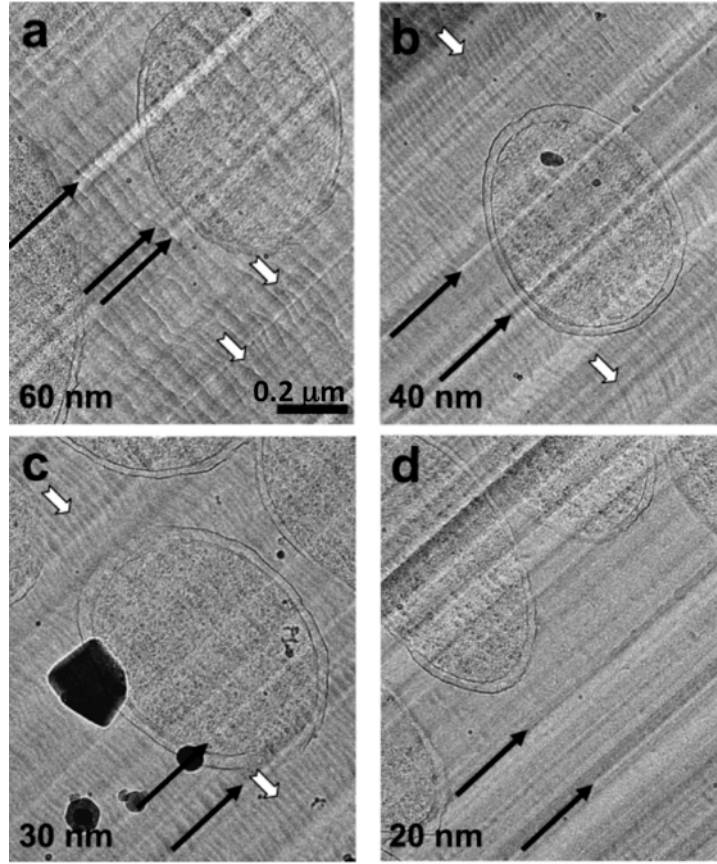


Figure 6: Progressive reduction of crevasse formation with reduction in section thickness. (a–d) Projection images of a 60-nm-thick section (a), 40-nm-thick section (b), 30-nm-thick section (c) and 20-nm-thick section (d) of frozen-hydrated wild-type *E. coli* cells grown in LB medium. Black arrows point to knife marks and white notched arrows to crevasses. All sections were obtained using a 25° cryo-diamond knife [14].

## 2.4 CURRENT STATE OF THE ART

### 2.4.1 FIB Slice-and-View

A dual beam (DB) focused ion beam (FIB) scanning electron microscope (SEM) uses a beam of focused Ga<sup>+</sup> ions to mill away parts of the sample leaving few defects and is usually used in

material science applications to make TEM samples or patterning silicon wafers (figure 7) [44]. The FIB can be used for site specific imaging of the interior of cellular and tissue specimens. This can allow a spatial resolution an order of magnitude better than optical microscopy (0.1-1  $\mu\text{m}$ ). This allows us to use a technique called “slice and view”, which is a technique based on using a FIB to create a cut at a designated site in the specimen. The cuts are then followed by viewing the newly generated surface with an SEM. The iteration of these two steps results in the generation of a series of surface maps of the specimen at regularly spaced intervals, which can be converted into a 3D map of the specimen (figure 8). This series of surface maps can then be computationally assembled into a volume representation of the specimen [8]. This technique has been used to explore the digestive gland epithelium cells of *Porcellio scaber* [4], atherosclerotic tissue [5] and HIV infected macrophages [6].

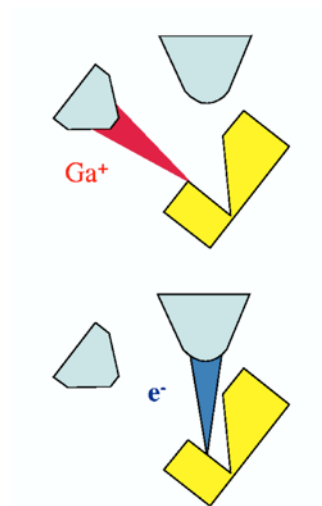


**Figure 7:**Schematic depicting the principle of FIB milling and SEM imaging in a dual beam electron microscope. The ion source (red, left) and the electron source (blue, top) are arranged at an angle allowing the ion beam ( $\text{Ga}^+$ ) to remove material from the surface of specimen (yellow) such that it can be imaged by the scanning electron beam ( $e^-$ ). As a result, a trench is generated, thus enabling imaging of the interior of the specimen. As shown, the exposed surface is parallel to the plane of the ion beam, and at an angle of  $52 \pm 2^\circ$  to the electron beam [8].

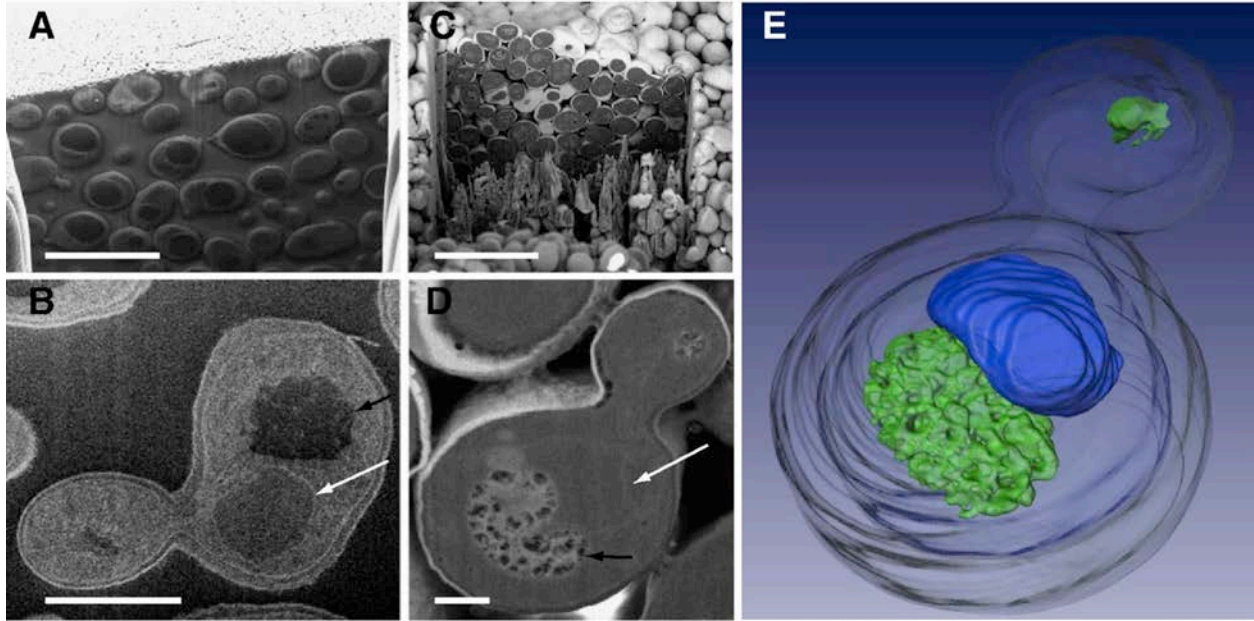


**Figure 8: 2D and 3D imaging of yeast cells by scanning electron microscopy. Scanning images of cross- sections of plastic-embedded (A and B) and critical point-dried yeast cells (C and D) at low (A and C) and high (B and D) magnification. Resin surface (A) and yeast pellet surface (B) were coated with platinum (white) prior focused ion beam milling. The long white arrows point to the location of the nuclear membrane in the budding yeast cells shown in (B and D), and the short white arrows point to the locations of the vacuoles, which appear black in (A and B) and white in (C and D). (E) 3D visualization of critical point-dried yeast cells was accomplished by iterative focused ion beam milling and scanning electron microscope imaging: segmented rendering of 3D volume displaying cell wall (gray envelope), the vacuolar region (green), and the nucleus (blue) of an individual, budding yeast cell. Scale bars: (A and C) 10  $\mu\text{m}$ , (B) 2  $\mu\text{m}$ , (D) 0.5  $\mu\text{m}$  [8].**

There are some drawbacks to using this technique. Firstly, there are filament and ridge like artifacts, which are a consequence of nonuniform milling, the melting effect, redeposition of the milled material on the surface and implantation of gallium ions. Secondly, the contrast visible in the images recorded in critical point-dried and plastic embedded cells is from the distribution of stain (osmium and uranyl acetate) rather than intrinsic contrast of cellular material. It is easier

in these studies to look at the absence of material, such as in structures containing pores, than to look for contrast in the cellular material [4].

The FIB slice and view technique can also be applied to samples that have been cryogenically frozen. Marco has shown that vitrified specimens can be milled using a low current beam (<50 pA) and still remain vitreous [44]. Frozen hydrated samples examined by cryo-SEM demonstrate superior preservation compared with chemically fixed and dried specimens because they retain all or most of their water, which allows the cells to be imaged much closer to how they are observed in their native environment [7].

When doing a cryo-slice and view technique, the samples are rapidly frozen (usually plunge frozen). Samples are then transferred to a cryo-preparation chamber where they can be sputter coated with a conductive layer. They are then placed into the main FIB chamber, where the milling and SEM imaging can take place, similar to the way it is done in plastic fixed samples. In the cryo-slice and view samples there are very many contrast problems, more so than in fixed samples. In figure 9(a and b), cryogenically frozen and milled samples can be seen to have significantly less contrast than those that have been stained and fixed (figure 8). One approach to solve the contrast problems is to locally sublime the ice present at the surface transiently raising the temperature of the specimen. This enhances the contrast leading to a sharpening of membrane features (figure 9(c and d)). The most noticeable artifact from milling is streaks appearing on the specimen surface along the milling direction. These artifacts vary from specimen to specimen, suggesting that specimen preparation and composition may influence the behavior. Metal deposition can be used, however it is difficult to achieve at cryogenic temperatures since the organo platinum compound condenses on the sample prior to decomposition by the ion beam [8], [7].

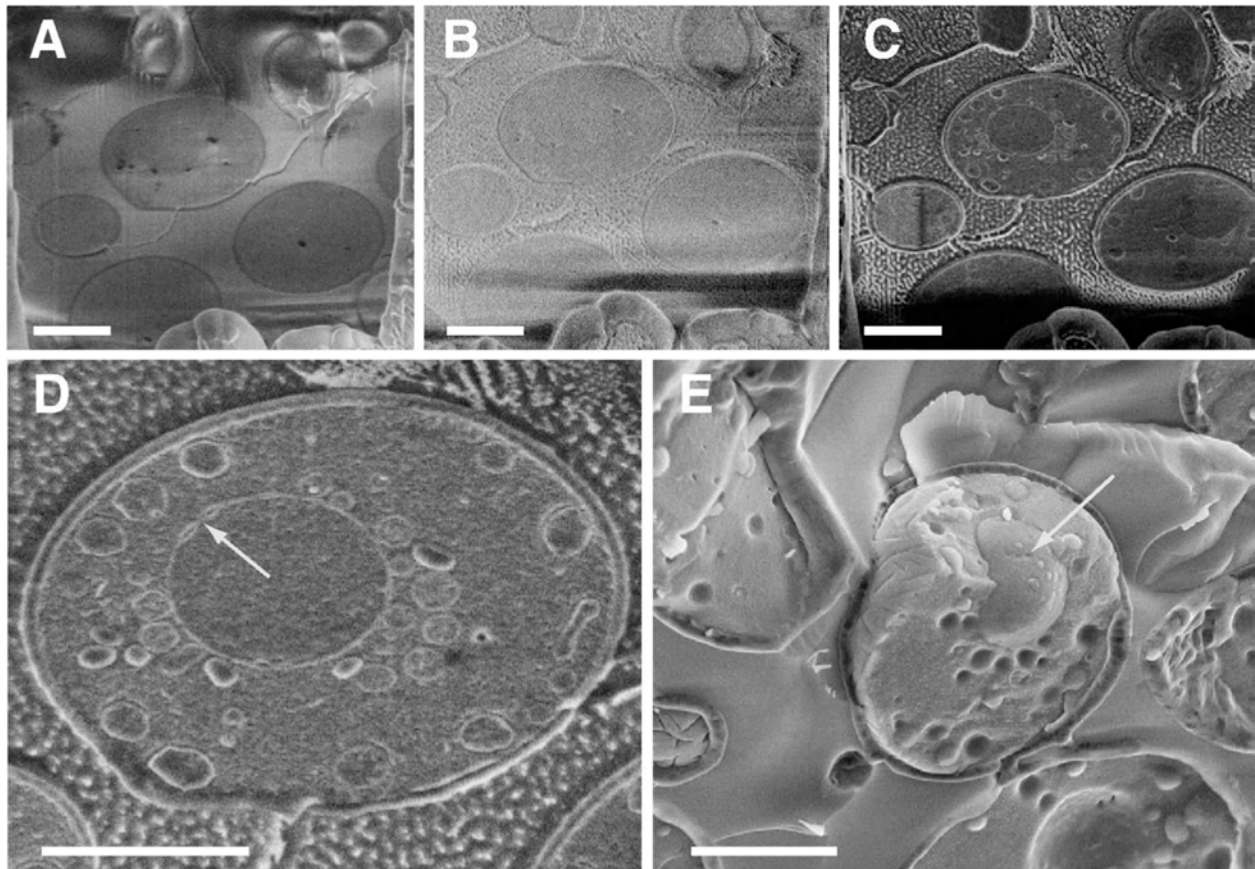


**Figure 9: Scanning electron microscope images of yeast cells plunge-frozen in liquid nitrogen and imaged at  $-140^{\circ}\text{C}$ . (A–C) Surface images generated by focused ion beam milling depicting progression in the sublimation process initiated by transiently raising the specimen temperature; (D) view of the crosssection of an individual yeast cell exposed by focused ion beam milling and contrasted by sublimation and coating with platinum and palladium. Arrow points to the location of a pore in the nuclear membrane. (E) Scanning electron microscope image of freeze-fractured, platinum–palladium coated yeast cells. Arrow indicates location of nuclear pore. Scale bars:  $2\ \mu\text{m}$  [8].**

In our research, we set out to try to perform a slice and view technique on *E. coli* cells embedded in a plastic resin. We aimed to reconstruct a 3D representation of the *E. coli* cells during their life cycles after expressing a viral protein encoded by a gene called the “E Gene”. By adding the chemical, IGA we induced the E gene expression. This gene expression causes the

bacterial cells to lyse. After the cells lyse there is only the outer cellular wall left. These shells collapse in on themselves and make 3D imaging very difficult. Using slice and view, we are able to keep the cells in the resin and give them some stability. By looking at the cells at different points after the E gene expression has been induced, we hope to get a good idea of what happens structurally when the cells lyse.

### **2.4.2 Cryo-FIB Milling**

Recently, it has been shown that a focused ion beam (FIB) can be used to thin biological samples [45], [46]. It has been shown that using a FIB to mill away ice at cryogenic temperatures and low current ( $<50$  pA) does not cause the sample to devitrify, which is very important in this technique, because devitrification will disrupt the structure of the cell [47]. Biological cells embedded in the ice can also be milled using the FIB under cryogenic temperatures. So far, it has been shown that yeast [46] and *E. coli* cells can be milled for use in tomography [45]. In these studies, a TEM grid with cells plunge frozen in suspension were loaded into the FIB, where they were milled at low currents and glancing angles to create very thin specimens that are electron transparent. Figure 10 shows a schematic of possible milling techniques to create cryo-TEM specimens. There have still been some reported problems concerning contamination and frost, as well as ice that is not optimum for milling [45], [46]. Also, thus far larger cells have yet to be examined using a cryo-FIB.

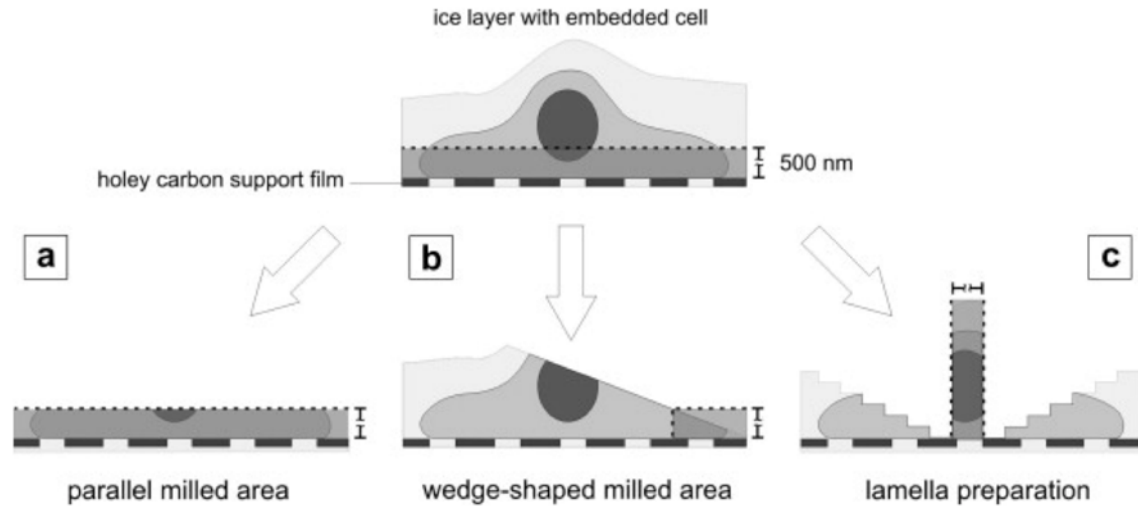


**Figure 10: Illustration of possible FIB-milling strategies for vitrified cellular samples. The frozen cell is attached to the carbon support film of an EM grid and embedded in a vitreous ice layer. A thin layer (delineated by the dashed line) represents the specimen thickness appropriate for cryo-electron tomography (<500 nm). (a) Parallel milling: the incident angle of the ion beam is parallel to the EM grid surface. This approach usually involves halving a frozen grid and is demanding, as subsequent transfers with the weakened grid half are necessary. (b) Wedge-shaped milling: the ion beam impinges on the frozen specimen at oblique or ‘grazing’ angles. This approach is the most feasible approach demonstrated thus far, as it can be performed without physically cutting the EM grid. (c) Cryo-lamella preparation: the frozen specimen is milled to expose a thin lamella, thereby preserving cellular features along the z-axis but necessitating physical removal and re-orientation of the lamella for TEM. At present a lift-out option for cryogenic lamella preparations is not available [45].**

In this research, we started by testing our equipment and techniques on *E. coli* cells before moving on to larger HeLa cells. In the following sections, we compare and contrast the difficulties of milling large mammalian cells as opposed to small bacterial cells.

## **3.0 EXPERIMENTAL METHODS**

### **3.1 FIB SLICE AND VIEW**

#### **3.1.1 Cell preparation for FIB slice and view**

The *E. coli* cells used for this experiment were engineered to express a viral protein encoded by a gene called the E gene. This gene causes the bacterial cell membranes to lyse and leads to cell death. The gene was carried in a plasmid and under tight control. Adding the chemical, IGA, to the bacterial cells, induced the E gene expression. A number of samples were created at different time points after the E gene was induced in order to observe the state of the cells all along the cycle.

The initial sample preparation was performed in the Structural Biology department at the University of Pittsburgh, School of Medicine. Previously frozen samples were warmed up from -196°C to -90°C in precooled (-90°C) 1% OsO<sub>4</sub> (EMS) and 0.1% Uranyl Acetate mixture dissolved in acetone to stain the cells. Substitution of the cells took three days at -90 °C with a brief daily agitation for each sample. The samples were then gradually warmed up to room temperature over a time span of 18 hours and subsequently rinsed in acetone for further resin infiltration. Generally the samples were fixed in a solution of 2.5% glutaraldehyde in 0.1 M PBS. A 1% OsO<sub>4</sub> solution with 0.1% potassium ferricyanide was used to post-fix the samples. The

samples were rinsed in PBS, and dehydrated through a graded series of ethanol steps and then finally embedded in Epon.

The resin blocks were formed in a pyramidal cone shape, with the cell pellets located in the tip. The area where the cells were located was flattened using a diamond knife, so that the imaging area was flat when put into the FIB. The samples were then coated with a thin layer of palladium approximately 2 $\mu$ m thick to ensure good electron conduction in the FIB. The blocks were then attached to an SEM stub using carbon tape and silver paint.

### **3.1.2 FIB slice and view milling**

The sample was then loaded into the Seiko Instruments SMI3050SE FIB-SEM with Oxford Instruments Inca XEDS (figure 11(b)). Once the sample was in the FIB, Tungsten was deposited in a 75x75x1  $\mu$ m square on top of the resin in the approximate area containing the E. coli cells using a current of 15.3 nA. This deposition smoothed the surface of the resin so that the mill surface was as smooth as possible in order to ensure a good SEM image of the mill face. Next, a sloping cut of 80x100x8  $\mu$ m was made leading up to the deposited square as seen in figure 11 using a large beam size of 7.6 nA. This creates the trench that allows us to use the SEM to view the interior of the sample where the cells have been embedded. Then, a series of thin, fine slices are made using a lower dose beam with a current of .74 nA in order to ensure that the face of the viewable area is nice and smooth. After each slice, an SEM image was taken of the surface. After a thickness of approximately 2 $\mu$ m has been milled and the images have been taken, they can then be put into a computer program that can reconstruct the cell volumes.

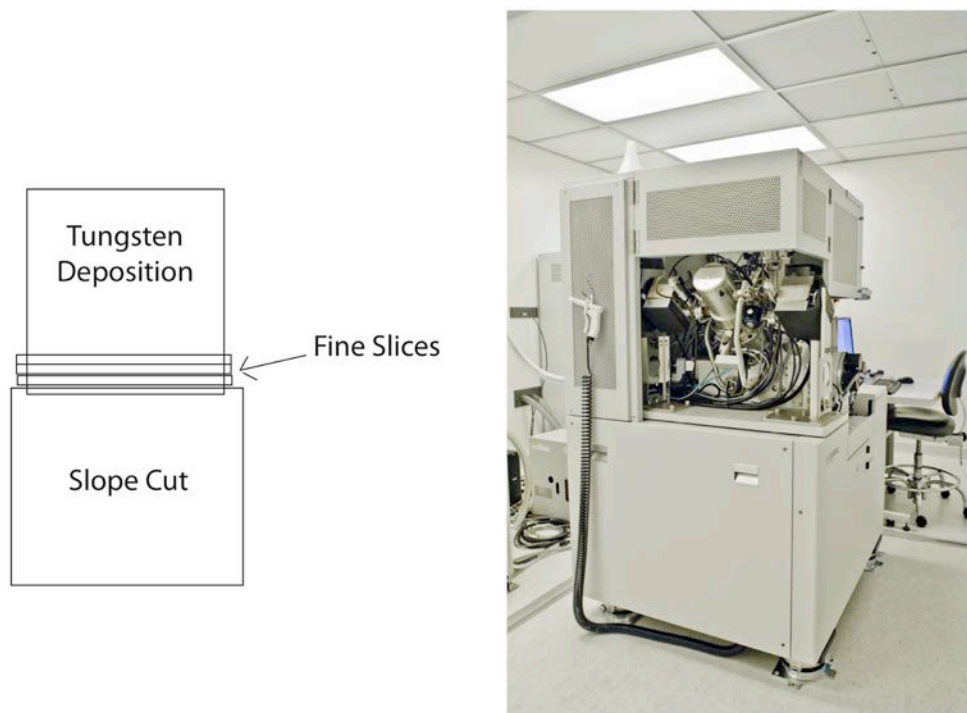


**Figure 11: FIB slice and view. (a) Schematic of the placement of the individual mills for the slice and view technique. The tungsten deposition is placed at the top and then a slope cut is done leading up to the deposition. The fine slices are then made at the interface between the large cut and the tungsten deposition. (b) Seico FIB system located at the University of Pittsburgh Nanoscale Fabrication and Characterization Facility (NFCF).**

## **3.2 CRYO-EM**

### **3.2.1 Cell preparation for cryo-FIB/TEM**

The initial sample preparation was carried out in the Structural Biology Department of the University of Pittsburgh School of Medicine. Wild-type K12 E. coli cells were grown in LB broth (10 % tryptone, 5 % yeast extract and 10 % NaCl). Starter cultures were grown overnight

at 34°C with 280 rpm shaking to an approximate optical density of 2.0 at 600 nm. Overnight cultures were diluted 1/40 into the same media and allowed to grow to an optical density of 0.5-0.6 at 600 nm. *E. coli* cells (3-5  $\mu$ l) were withdrawn directly from cultures, mixed with 15 nm gold beads (2  $\mu$ l), and placed on R2/2 Quantifoil grids (Micro Tools GmbH, Germany). The grids were manually blotted from the back side of the grid with a filter paper and plunge-frozen in liquid ethane using a home-made manual gravity plunger. The frozen grids were loaded onto the modified Polara cartridges (FEI, Hillsboro, OR) with cell side facing up and stored in liquid nitrogen for future use.

HeLa cells were cultured at 37 °C with 5 % CO<sub>2</sub> in DMEM containing 4.5 g/L L-glutamine and glucose (Lonza Group Ltd, Basel, Switzerland), 10% heat inactivated fetal calf serum, 100 units/ml penicillin, and 100  $\mu$ g/ml streptomycin (Invitrogen Corporation, Carlsbad, CA). Cultures at ~ 80 % confluence were routinely split 1:5 in 60 mm culture dishes. Cells were centrifuged at 1000x g and plated onto the gold R2/2 Quantifoil finder EM grids (Quantifoil Micro Tools GmbH, Jena, Germany) at a density of 2 x 10<sup>4</sup> cells/ml (total 2 ml culture) in glass-bottom culture dishes (MatTek Corporation, Ashland, MA). The gold EM grids were disinfected under UV light for 2 hours and coated with 50  $\mu$ g/ml fibronectin (Sigma) before use. DIC images of cultured HeLa cells were recorded with an Olympus IX71 microscope using a 20x objective lens before plunge-freezing. 15 nm gold beads (4 $\mu$ l) were applied to the cell culture on EM grids, blotted with filter papers, and plunged into liquid ethane for rapid vitrification using an FEI Vitrobot (FEI, Hillsboro, OR). The frozen grids were loaded onto the modified Polara cartridges with cell side facing up and stored in liquid nitrogen for future use.

### 3.2.2 Cryo-FIB Milling

It is important to keep the samples under liquid nitrogen at all times. If the samples come to a temperature above approximately  $-150^{\circ}\text{C}$ , the ice begins to devitrify. In order to keep the samples below this temperature, we kept the samples under liquid nitrogen during transport from the initial freezing and into the FIB and then during transport from the FIB and into the TEM. As long as the samples are kept at liquid nitrogen temperatures, they can last indefinitely.

For FIB milling, an FEI Quanta 200 3D DualBeam FIB/SEM (FEI Corp., OR) (figure 12(b)) equipped with a Quorum Polarprep 200T Cryo-Transfer Station (figure 12(a)) and a Quorum PP7465 Dual Slusher System (Quorum Technologies Ltd, East Sussex, UK) was used. A specialized shutter was designed by the University of Pittsburgh School of Medicine Machine Shop (figure 13(a-c)) for use on the cold stage of the Quorum PolarPrep. There are many advantages to using this shuttle design. Since the Polara TEM requires the use of cartridges in the loading mechanism instead of just electron microscopy grids, we are able to design the shuttle to accept the cartridge too. This means that the grid is only handled during the initial loading of the grid into the cartridge and reduces the contamination and damage problems usually associated with loading and unloading an EM grid.

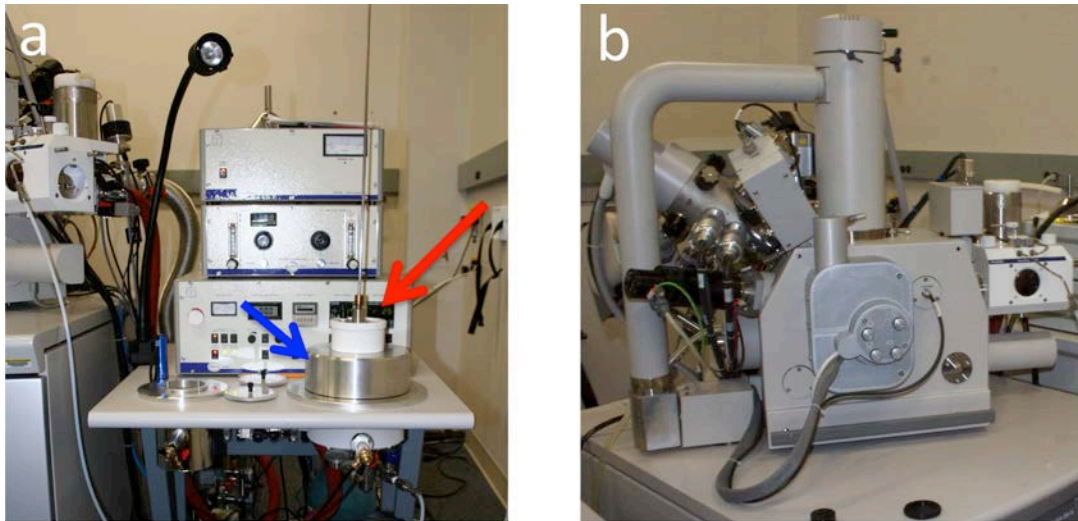


**Figure 12: Cryo-FIB loading and milling equipment. (a) The Quorum PolarPrep 200T Cryo Transfer Station The blue arrow indicates the slusher and the red arrow indicates the transfer arm. (b) The FEI Quanta 200 3D DualBeam FIB/SEM, both located at Penn State University Materials Research Institute**

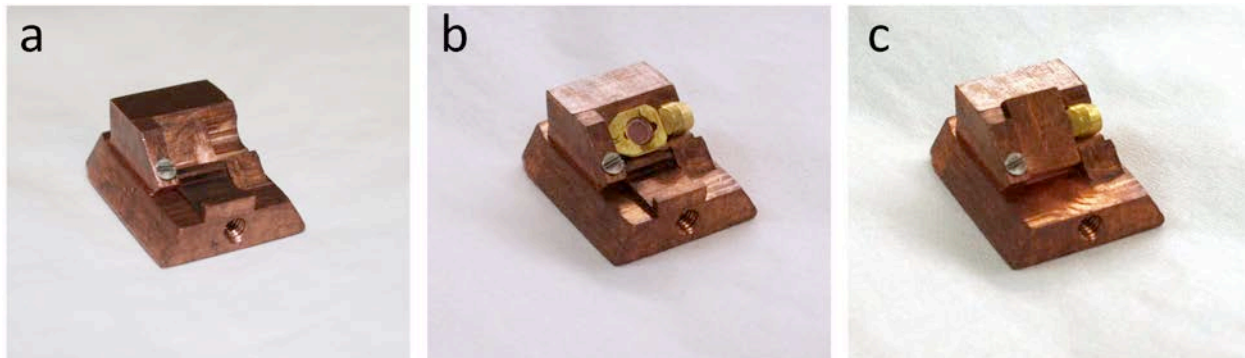


**Figure 13: Cryo-FIB milling shuttle. (a) Shuttle designed to accept Polara TEM cartridges and fit into the Quanta 200 3D Dual Beam system. (b) Polara cartridge inserted into specialized shuttle. (c) Shutter used to reduce contamination and frost protecting the Polara cartridge.**

The design of the shuttle also keeps the grids in the same orientation from FIB to the TEM. The axis from the FIB to the TEM is rotated 90° clockwise and is shown in figure 14 (b and c). This allows for easier acquisition of the tomography tilt series. The rotation also makes finding the mills in the TEM much easier. Another important advantage of using this shuttle

design is that the shuttle is also designed with a shutter mechanism that protects the grid from contamination during transfer into and out of the DB as seen in figure 12 (b and c), which eliminates a very large problem found in cryo-FIB milling. Another very important factor in cryo-FIB milling is the milling angle. The smaller the angle between the sample and the FIB beam, the thinner the sample and the more useable area for tomography (discussed more in depth in the following sections). The Polara cartridge itself was also modified slightly with small channels cut into the sides to allow for shallower milling angles and can be seen in figure 14 (a) compared to the standard Polara cartridge.

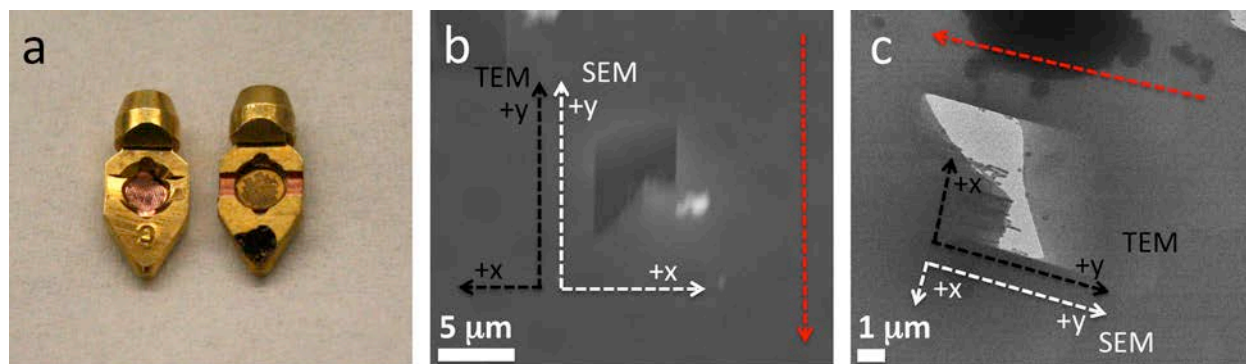


**Figure 14: Milling equipment and milling orientations. (a) Comparison of the regular Polara cartridge (left) and specialized cartridge with channels to allow for lower milling angle. (b) SEM image of a mill, showing the x and y axis in the SEM (white) and TEM (black), the red arrow indicates milling direction. (c) TEM image of a mill, also showing the x and y axis of the SEM (white) and TEM (black), the red arrow indicates milling direction. Note the rotation of 90° between the TEM and SEM images.**

The frozen EM grids are loaded into Polara cartridges and then loaded onto the shuttle while immersed in liquid nitrogen. The shuttle is loaded into the polar prep transfer station and kept under liquid nitrogen. It is important to use coated Styrofoam cups in the transfer station because the holes in regular Styrofoam allow air to enter the liquid nitrogen and condense, which causes contamination in the liquid nitrogen, which can then be transferred to the sample. Then

the transfer station (figure 12 (a), blue arrow) is pumped down until the liquid nitrogen is slushed and the shuttle is retracted into the transfer arm (figure 12 (a), red arrow) and a small seal is formed to protect the sample during transfer to the FIB prep chamber.

The transfer arm is attached to the prep gate valve and pumped down before insertion into the prep chamber. The sample is not in contact with liquid nitrogen for approximately 30 seconds while the valve is pumped down. The seal that was formed in the transfer station helps protect the sample from devitrification during this time. Inside the prep chamber is a small cryo stage kept at approximately  $-180^{\circ}$  C. After the shuttle is successfully transferred, the prep chamber is pumped down to  $10^{-4}$  mbar and then the gate valve between the prep chamber and main FIB chamber is opened and the shuttle is transferred to the cold stage.

The dual beam contains both a FIB and SEM column that are focused at the same point on the sample but  $52^{\circ}$  apart as shown in figure 15 (a and b). The sample is then tilted to approximately  $10^{\circ}$  with respect to the axis of the FIB column. It is important that this angle is as small as possible because the smaller this milling angle, the larger the available viewing area in the TEM, as shown in figure 15 (b). Also, a smaller angle will produce a thinner sample area, which is ideal for tomography. However, the sample must still be viewable in the FIB, so that the milling area can be selected and to ensure that the beam is not blocked by the sample.

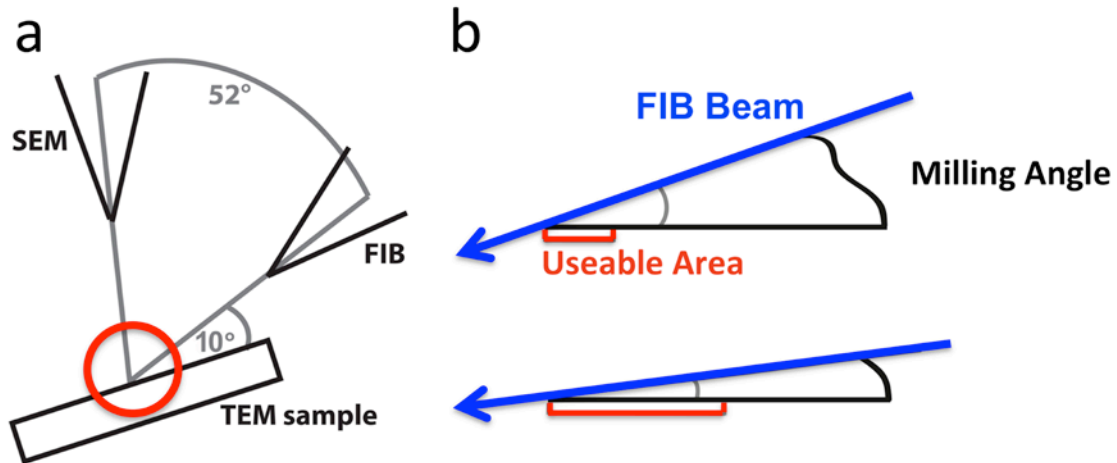


**Figure 15: Cryo-FIB sample and milling schematic. (a) Setup of the dual beam system. (b) Magnification of the red circle indicated in figure (a). The blue arrows indicate the FIB beam and the red area indicates the useable area for TEM imaging, the smaller the milling angle, the larger the useable area.**

After the sample has been properly situated with respect to the FIB and the SEM, milling begins. A milling current of 10-30 pA was used depending on the specimen thickness and an accelerating voltage of 30 kV. Thinner samples, such as *E. coli* milled much faster (approximately 30 seconds to a minute) and therefore only needed a current of 10 pA. The larger specimens, like HeLa cells, required a higher current of 30 pA and a longer time of about 20 minutes per mill due to their increased thickness. The milled area was approximately  $1 \times 5 \mu\text{m}$ , which allows for a focusing and tracking region in the TEM. As stated above, the milling angle was approximately  $9\text{-}12^\circ$  to ensure a thin sample. The SEM images were obtained using an accelerating voltage of 10 kV and 0.45 nA current.

### 3.2.3 Cryo-TEM and Cryo-ET

After cryo-FIB processing, EM cartridges were stored in liquid nitrogen before they were examined by cryo-EM with an FEI Polara G3 (FEI Corp., OR.) (figure 16) TEM equipped with a field emission gun and a Gatan 4K x 4K CCD camera (Gatan, Inc., Warrendale, PA). The FIB-milled regions were first located in low magnification (170 x) EM projection images. Low dose ( $20 \text{ e}^-/\text{\AA}^2$ ) projection images of the identified regions of interest were recorded on a CCD camera at a nominal magnification of 50,000x and under-focus values ranging 2-4  $\mu\text{m}$ . For cryo-ET, a series of low dose projection images of the milled regions were recorded at tilt angles ranging from  $\sim 70^\circ$  to  $70^\circ$ , depending on the topography of the sample, at a nominal magnification of 39,000x (pixel size=0.31nm), with an under-focus value of 10  $\mu\text{m}$ . The electron dose per frame was kept under  $2 \text{ e}^-/\text{\AA}^2$ , with a total dose of about  $110 \text{ e}^-/\text{\AA}^2$ . Tilt series were aligned using 15 nm gold fiducial beads and refined to standard deviations below 0.8.



**Figure 16: FEI Polara TEM located in the structural biology department, University of Pittsburgh**

### **3.2.4 Tomogram Reconstruction**

A weighted back-projection algorithm, as implemented in the IMOD reconstruction package [48], was used to convert the information present in the series of tilted projection images into 3D density maps (tomograms). The tilt series was aligned using the gold fiducial markers in the E. coli samples. In the HeLa samples, there were not enough gold markers present to be able to track the samples. In this case, manual aligning was used to align the tilt series. Diffusion and low pass Fourier filters were also applied in the final reconstruction in order to increase contrast and define features.

The images needed to be compressed after the initial reconstruction because the files were very large and the computers could not handle the file sizes. The 3D tomographic volumes were visualized and segmented in the environment of the program Amira (TGS Inc., San Diego, Calif.). The segmentation was done by hand, using the paintbrush selection tool in order to be sure the correct features were being highlighted. The selections were then entered into the program and the new surfaces were generated and colored according to what features they represented.

## 4.0 RESULTS AND DISCUSSION

### 4.1 FIB SLICE AND VIEW

#### 4.1.1 Milling Results

We were able to perform the sloping cut up to the face of where the bacteria cells were located. It can be seen in figure 17 that the cells were exposed after doing the slope cut and then performing a fine cut using a lower dose beam to “polish” the surface. The *E. coli* cells are visible in a high magnification image located in the inset image in figure 17 and the cell structure can be seen in a decent amount of detail and with some contrast, including the double walled structure of the *E. coli* cells.

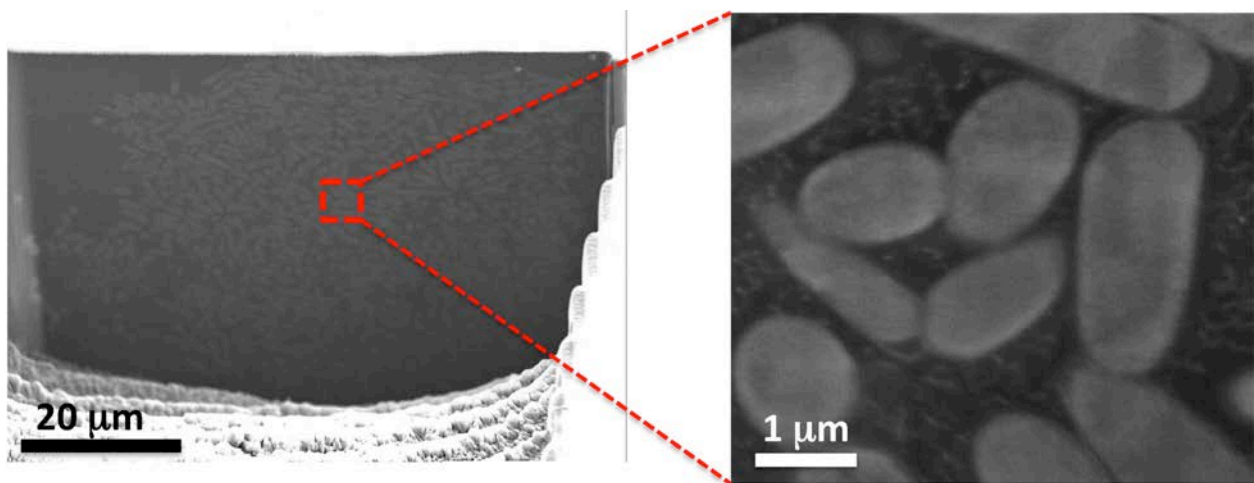


**Figure 17: FIB slice and view overview. The red box indicates an area that is blown up in the inset image. The cells pictures in the inset can be seen with good detail and contrast.**

We were also able to obtain a series of slices of each of the 5-minute (progression shown in figure 18) and 25 minute samples (progression shown in figure 19). The slices were approximately 7.5 nm thick; the images shown in figures 19 and 20 are from every fourth mill, meaning the slices are approximately 30 nm apart. It can be seen in figure 18 and 19, as we progress through the sample that cells appear to grow or shrink, which indicates that we successfully progressed through the sample. In the 5-minute sample, we are also able to see the double walled structure of the bacteria cells, which means the resolution is good. One problem we encountered in this sample was the prevalence of streaking on the surface of the imaging area. This streaking appears to be getting worse as the mills progress through the sample. Another problem was that after most mills, the sample needed to be refocused and the contrast and brightness adjusted. The contrast and brightness was not a large problem in this sample, but the focusing requires at least a small area that will be exposed to more damage than the rest of the surface. This refocusing left a small square on the left side that appears to be raised up from the rest of the sample. These artifacts can interfere with the computer reconstruction.

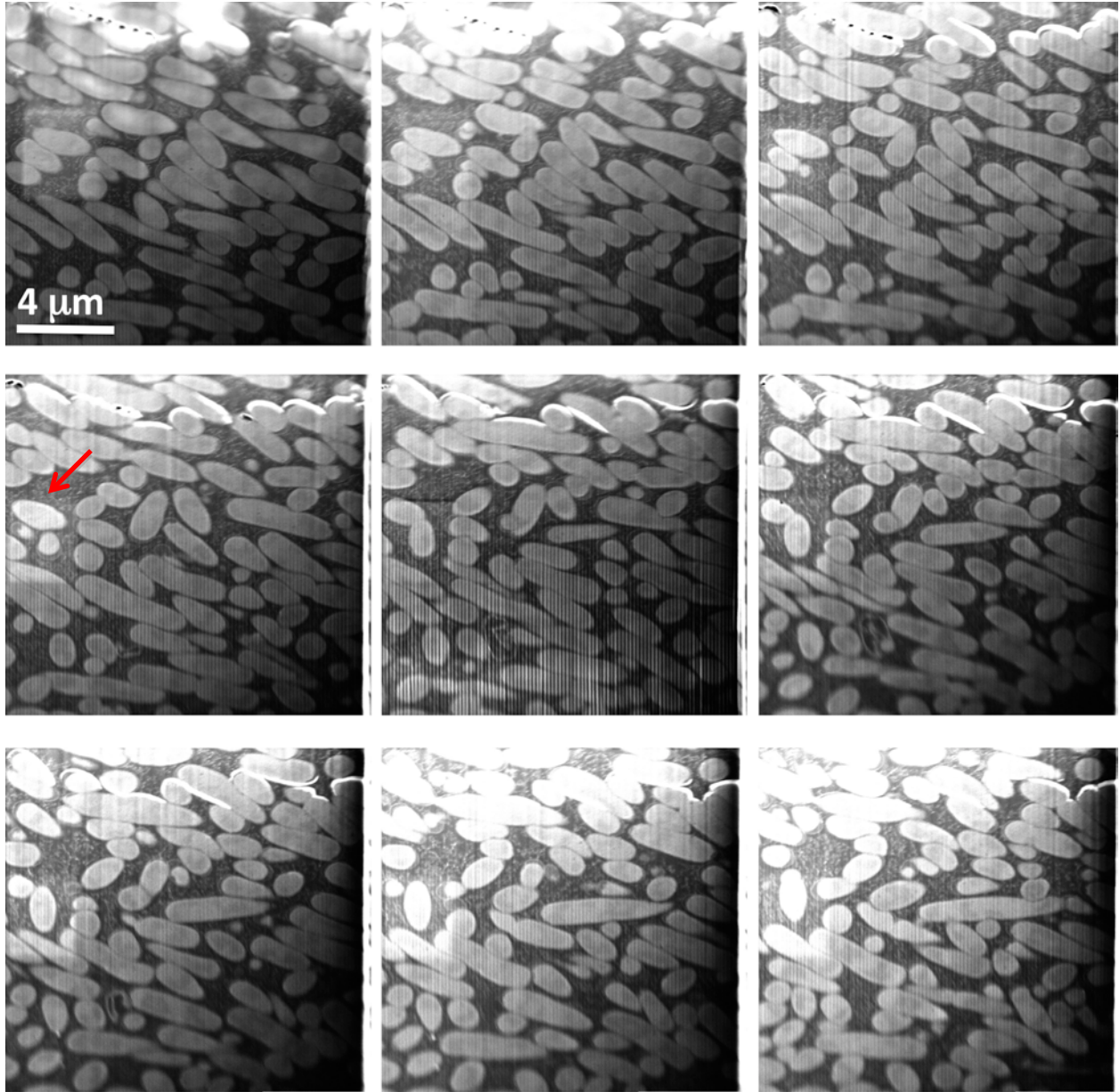


**Figure 18: Slices from 5-minute sample. Each image is four slices apart, which is approximately 40 nm. As the slices progress through the cell, the streaking on the bottom half of the image can be seen getting worse. The red arrow indicates the square on the left side of the images caused by the refocusing required after most slices.**

In the 25-minute sample (figure 19), we can see the lysed cell walls, which appear as empty cells, as well as cells that are still intact. In this sample, we did have trouble getting the

contrast and brightness correct, so they sometimes changed from image to image, with some images having parts that are very bright, while others are very dark. There were also problems in this sample with streaking disrupting the image, as well as portions of the face that are not completely milled. Another problem we had with this sample was stage drift. The sample was slowly moving to the right during the milling process. It was necessary to reposition the sample after every few mills in order to ensure that the cells we are imaging are present in every slice. This increases the number of times the images had to be refocused and the brightness and contrast adjusted, which adds more time to the process.

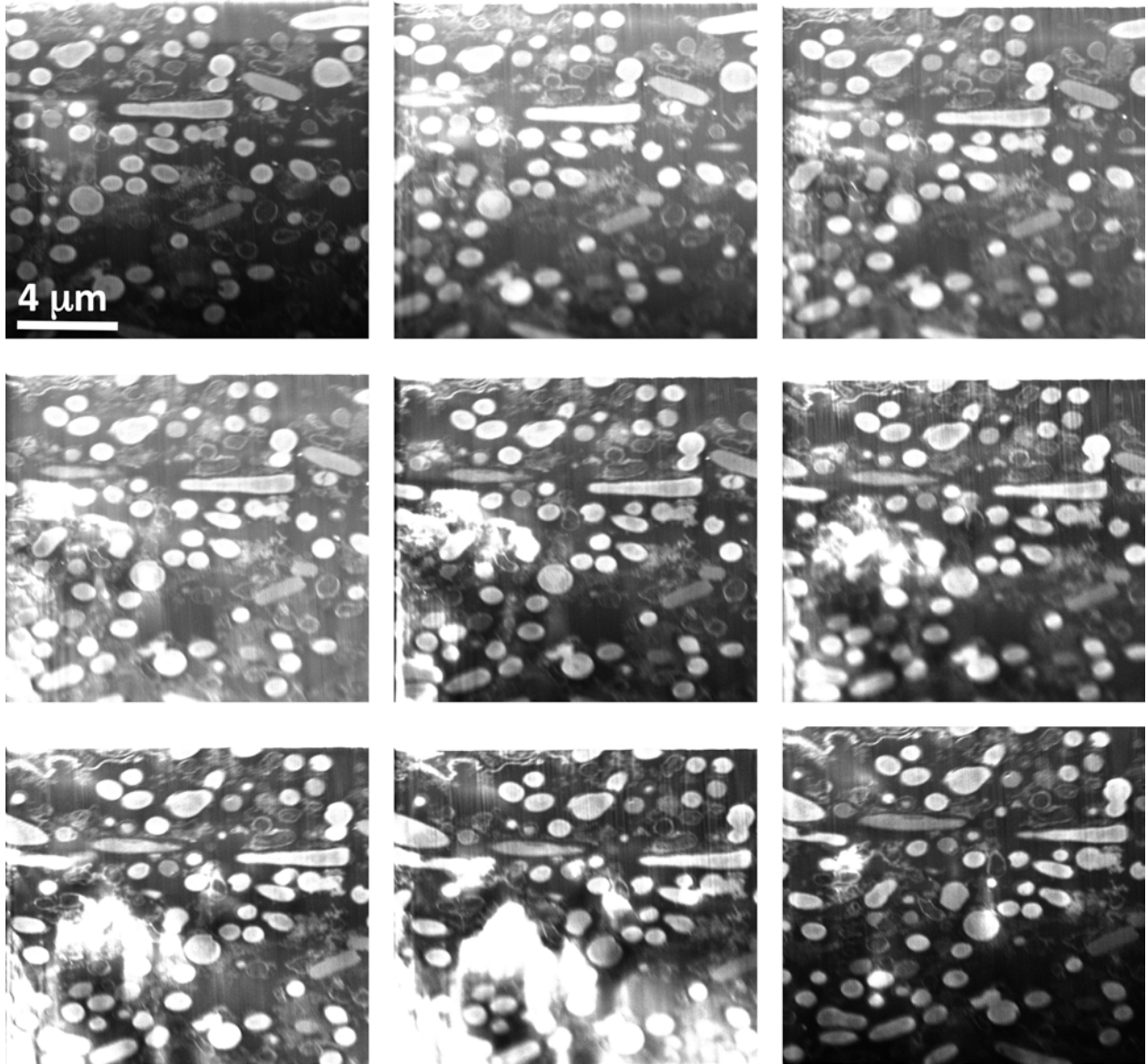


**Figure 19: 25-minute sample. Each image is four slices apart, which is approximately 40 nm. In this sample, there were many drifting problems, so the sample had to be repositioned after every few slices. The difference in position can be seen in the sequence of images. This sample also had some focusing and contrast issues, which distorts the final images.**

### 4.1.2 Discussion

Even though we were able to get good images from a few of the slices, we ran into many problems when trying to carry out these experiments. These problems included, stage drift, streaking, and time constraints. We tried to fix these problems using multiple solutions.

There was a lot of stage drift apparent in the FIB between subsequent slices. It was necessary to reposition the sample after a few slices so that we could keep the same cells viewable throughout the entire milling process. We could not find a good solution to this problem beyond manually repositioning the stage after a few slices. This increased the time and required additional focusing, which increased damage on the sample. In figure 18, a small square can be seen on the left of the image. This is where the fine focusing was performed and left artifacts. This artifact can interfere with the 3D reconstruction and cause artifacts to be present in the reconstruction that interfere with the structure of the cells.

Another problem found when trying to make thin slices, the samples exhibited a lot of streaking, which is a big problem when trying to perform FIB slice and view. These streaks can also cause problems when the computer program tries to reconstruct the image because the computer cannot accurately track the cells through the sample, as well as creating artifacts that obscure the final reconstruction. To combat the streaking issue, we tried using a thicker deposition of tungsten on the surface of the sample; however, this increased the time required for a single mill to 3 minutes and reduced the thickness of each mill. Coupled with the fact that each reconstruction must be comprised of many slices, the time required to mill each sample became very large.

The FIB located in the University of Pittsburgh, NCF does not have an automated setting, and so a user is required to sit with the specimens during the entire procedure. The

samples shown in figures 18 and 19 are each from a single eight-hour session. For a successful reconstruction, the mills must span a 2-3 $\mu$ m thickness (large enough to capture an entire cell both length and width). Each mill is approximately 5-7nm, with each slice taking 2-3 minutes to complete. This means that each sample requires a total milling time of approximately 22 hours, not including time for refocusing or brightness and contrast changes. This time will also increase as the thickness of the deposition layer increases due to increased milling time and thinner slices. The sample cannot be taken out in the middle of a run either because it is very difficult to realign the specimen once milling has begun. Also the exposed surface becomes dirty when exposed to air and needs to be polished with a fine beam before milling can resume. This will remove extra material and the spacing on the reconstruction will be incorrect.

In the end, this method of 3D reconstruction was abandoned because we were not able to come up with a method that created a streak free surface that did not require very large amounts of time. We did not move on to cryogenically frozen samples after working at room temperature, because the contrast is much lower in cryogenically frozen samples, and the streaking can be a bigger problem [8]. Also, the amount of time required to mill the specimens was very large. If we were to continue working with cryogenically frozen specimens, we would have to use an even lower milling current, which would increase the time for each slice even more. Therefore, we did not even attempt to try this technique with vitreous specimens. It was much more advantageous to move on to using cryo-FIB techniques to create TEM samples for cryo-ET and were much more successful in creating viable samples.

## 4.2 CRYO-EM

### 4.2.1 Design and Construction of the Cryo-FIB shuttle

Our goal is to obtain detailed, internal, 3D architectures of native cells, large mammalian cells in particular, at molecular resolution, using cryo-electron tomography (cryo-ET). Cryo-ET requires the specimen thickness to be less than 300 - 500 nm, since the apparent specimen thickness increases considerably during the acquisition of a tilted projection series. Previous efforts to use cryo-FIB to reduce bacterial cell thickness to a degree suitable for cryo-ET demonstrated its feasibility [45], [46]. To advance this technology for investigating the internal structure of larger cells and to improve the cryo-FIB process for efficient and easy use, we designed and constructed a cryo-FIB shuttle (figure 20) that directly accepts a cryo-EM specimen cartridge for subsequent 3D structural analysis without the need for transferring the EM grid, eliminating specimen deformation and damage produced during transfer. This integrated feature greatly enhances the performance of cryo-ET, since successful cryo-ET data acquisition critically depends on the flatness and integrity of the grid. The cryo-shuttle design is shown in detail in figure 11 and includes several important features: The specimen cartridge is recessed into the dove-tailed, copper FIB/SEM shuttle to ensure low specimen temperatures (-175°C to -185°C). It also includes a shutter mechanism that protects the grid from frost contamination during transfer into and out of a FIB/SEM system (Figure 13 (b and c) open or closed), and the specimen cartridge features cut-outs on both edges (Figure 14 (a)), allowing for shallow milling angles (10°) and a high angular tilting range ( $\pm 76^\circ$ ) for tomography.

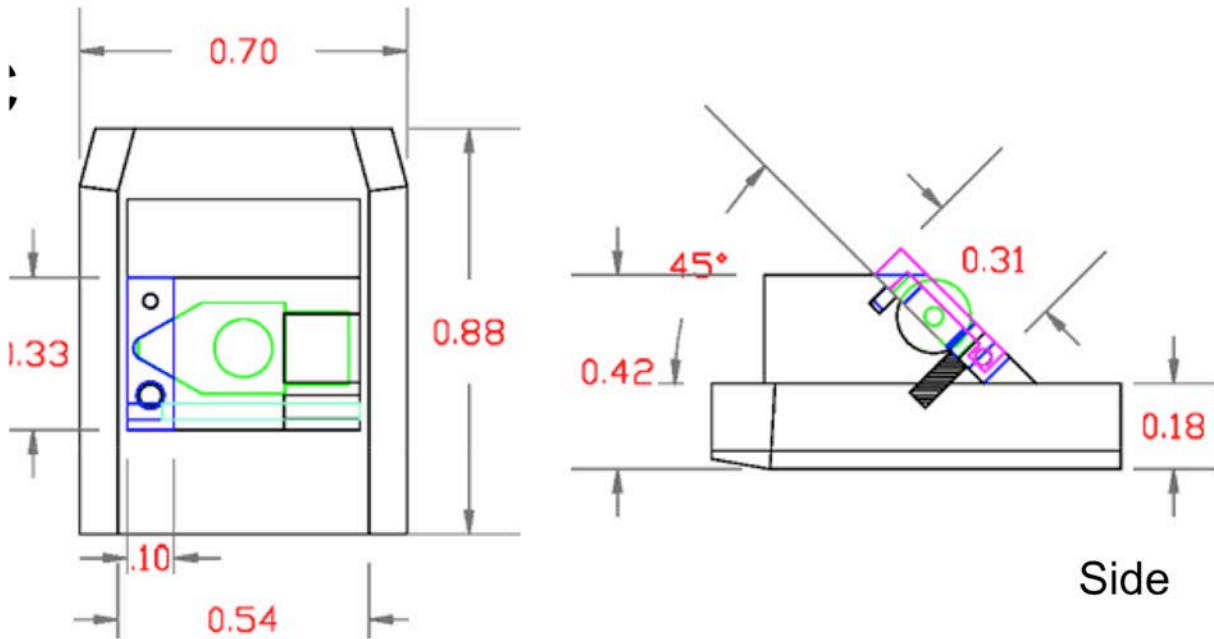


**Figure 20: Autocad drawing of the cryo-FIB shuttle as viewed from top (left) and side (right). Dimensions are marked in inches. The block face where the cartridge sits is at 45°. The specimen shutter (closed) is depicted in pink in the side view. (D) Schematic of the FIB and SEM beam set up in the DualBeam system. The angle between the SEM and FIB beams is 52°. The cryo-FIB shuttle was designed to allow a very shallow milling angle (10°).**

Taken together, our unique shuttle design has a number of advances: 1) It allows very shallow milling angles (10°) for generating large “transparent” sample areas for cryo-ET analysis [45]; 2) It has a built-in specimen shutter to protect the specimen and minimize ice contamination, resulting in near-frost-free transfer; 3) It includes an integrated specimen holder for stable specimen support, affording sequential FIB milling and cryo-ET to be performed on the same holder without sample transfer, thus, eliminating deformations of the fragile sample grid induced by gripping or clamping during grid transfer; 4) It maintains the grid in a fixed orientation in both cryo-FIB and cryo-ET; therefore, the FIB milling direction coincides with the tomographic specimen tilting direction, allowing for a perfect match of the FIB-thinned area with

the tomography imaging area during specimen tilting. Such a design makes 3D structural analysis of cryo-FIB processed specimens much more proficient and reproducible; 5) Most importantly, it allows for production of freely-suspended cell lamella: by applying two consecutive mills, either parallel or anti-parallel, one can create a specimen slab on the EM grid that is ready for cryo-ET analysis without the need for cryo-FIB “lift-out”. Such a FIB milling approach for specimen slabs is useful not only for biological specimens but also in the field of materials science, since it eliminates the difficulties associated with the FIB “lift-out” procedure and with specimen transfer across sample processing and imaging platforms.

## **4.2.2 Ice Quality**

The quality of the ice is very important in the final condition of the samples. The ice needs to stay vitreous throughout the milling and TEM processes in order for the samples to be viable for TEM and tomography. In cryogenic samples, crystalline ice can disrupt imaging of the fine structure of the cells. In our experiments, we observed three different types of "bad ice". Each type can indicate where in the process the sample came above temperature.

### **4.2.2.1 Granular Ice**

The first type of bad ice we observed was granular ice, which is characterized by small grains of ice as seen in figure 12. This happens when the sample comes close to the devitrification temperature but does not rise above it significantly or for a significant amount of time. Many times this can be caused by removing the sample from the liquid nitrogen for only a few minutes. This type of bad ice can be the most difficult to diagnose. Many times the sample was only in the devitrification zone for a few seconds before this ice formed. This happens when the sample

temperature was not monitored closely enough and the temperature raised a few degrees for a few seconds.

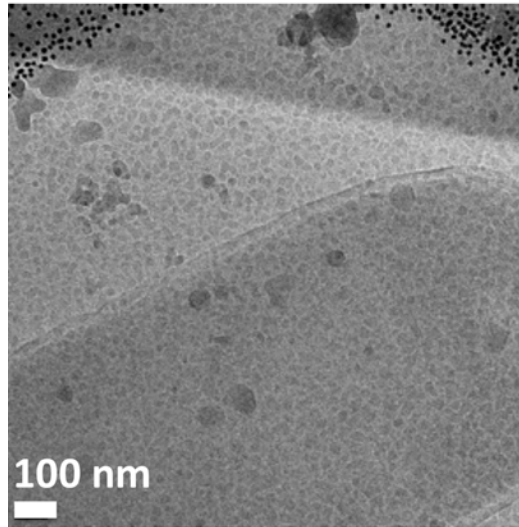


**Figure 21: Granular ice, characterized by small grains of devitrified ice.**

#### **4.2.2.2 Devitrified Ice**

The second type of bad ice is completely devitrified ice. This occurs when the sample has been above the devitrification temperature for a significant amount of time, usually a few minutes. These samples are characterized by large ice crystals that run into each other and can be seen to disrupt the structure of the target cells as shown in figure 22. We mainly observed this ice when there was a problem with the loading process.

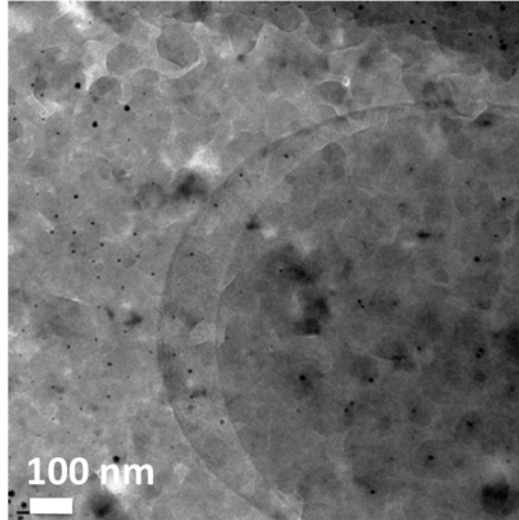


**Figure 22: Devitrified ice, characterized by large ice crystals that distort the internal structure of the cell.**

#### **4.2.2.3 Directional Ice**

Another possible type of ice that is caused by bad freezing is directional ice. The ice appears to have grown in a directional manner as shown in figure 23. This ice is caused by incomplete initial freezing, as evidenced by the directional freezing patterns. This ice indicates that the samples were not frozen quickly enough to give the ice an amorphous structure during the plunge freezing process and directional ice was able to grow.

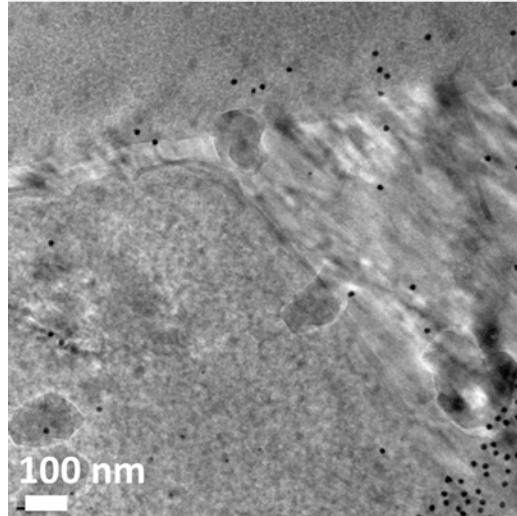


**Figure 23: Directional ice, characterized by ice that appears to grow in a certain direction, due to incomplete freezing during the plunge freezing process.**

#### **4.2.2.4 Good Ice**

Good ice is shown in figure 24. The ice appears to be completely gray and smooth. There is no evidence of any type of structure or crystal. This is the ideal ice for TEM and tomography because there are no ice crystals disrupting the structure of the cells. We found that in order to keep the ice devitrified, it was important to keep the FIB as cold as possible during the entire process. For our system, we were able to keep the FIB below  $-183^{\circ}\text{C}$  for the entire process. Keeping the samples as cold as possible (most times significantly below the devitrification temperature) gives the sample a buffer in which the sample can be transported between the FIB and liquid nitrogen without too much of an increase in temperature.

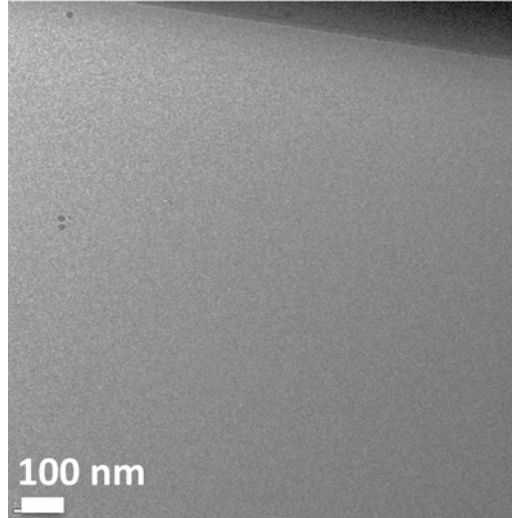


**Figure 24: Good ice, characterized by having no defects or crystallinity apparent.**

#### **4.2.2.5 Milling Artifacts**

In some of the milled samples, there are some artifacts present after the milling. The artifacts appear as small gray spots in the ice, which appear to have a regularity and pattern (figure 25 (b), white arrow). In what appears to be inside of the cells, these artifacts look like larger gray “blobs” (figure 25(b), black arrow). In figure 25(b and c) it can also be seen that the artifacts are only present in milled areas (figure 25(b), black and white arrows) and not present in unmilled sections (figure 25(c)). These artifacts could be due to milled material redepositing back on the milled surface. We know these artifacts are present only on the surface of the milled specimens because after tomography reconstruction, they are only present on the surface slices of the reconstruction. The artifacts are not present in all samples, and in general the quality of the milled regions of the *E. coli* cells was very good.

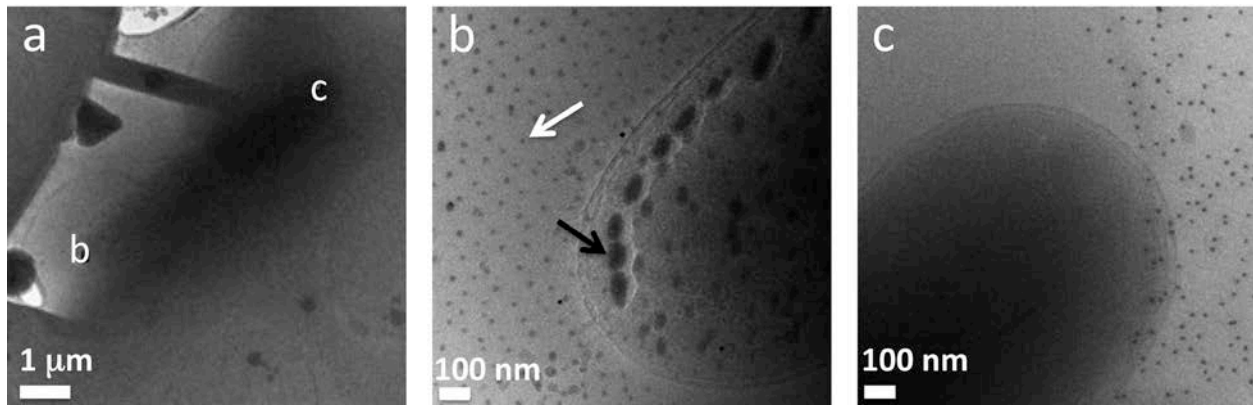


**Figure 25: Milling artifacts. (a) Overview of the milled region taken in the TEM. (b) The milled region indicated on image (a), the white arrow indicates the milling artifacts outside of the cell that appear to have some regularity, the black arrow indicates the "blob" like artifacts. (c) The unmilled region indicated on image (a). The dark black spots on the images are gold fiducial markers used for alignment.**

### **4.2.3 E. Coli**

The *E. coli* samples were initially used to determine the feasibility of our technique and as a baseline to compare milling of smaller cells, which has been performed before, to the milling of larger HeLa cells, which is the motivation for this research.

We first tested the performance of our cryo-FIB shuttle using plunge-frozen bacterial cells. Fresh *E. coli* cells growing in the log phase (OD at 600 nm was  $\sim 0.6$ ) were directly applied to the EM grid and plunge-frozen. The cryo-EM grids with frozen-hydrated cells were loaded into specimen cartridges, which were then mounted into the cryo-shuttle and imaged in the FIB/SEM system using the scanning electron beam and a secondary electron detector. The SEM images recorded with a beam current of 0.45 nA showed discernable *E. coli* cells before and after cryo-FIB milling (figure 26(a-c)), even without a platinum protection layer as previously required [45]. The good contrast made identification and milling of *E. coli* cells relatively easy

and efficient, resulting in high yields (>80%). Depending on the density of *E. coli* cells on the EM grid, typically 10-20 areas of interest could be selected for milling within a single grid square. Using a 30 keV, focused, gallium ion beam at an incident angle of 10°, with a relatively low ion current of 10 pA (dose rate 0.67 ions/nm<sup>2</sup>/sec), a thin (~400 nm), slightly wedge-shaped area, exposing *E. coli* cellular volume (figure 26(d and e)), was produced for cryo-ET in less than 1 minute of processing time. Under such low beam current conditions, the sample remained in its vitreous state after FIB milling, as indicated by the characteristic amorphous ice diffraction patterns recorded from the milled area (data not shown). The bacteria cell selected for subsequent tomographic analysis is indicated by white arrows in figure 26(a-d).

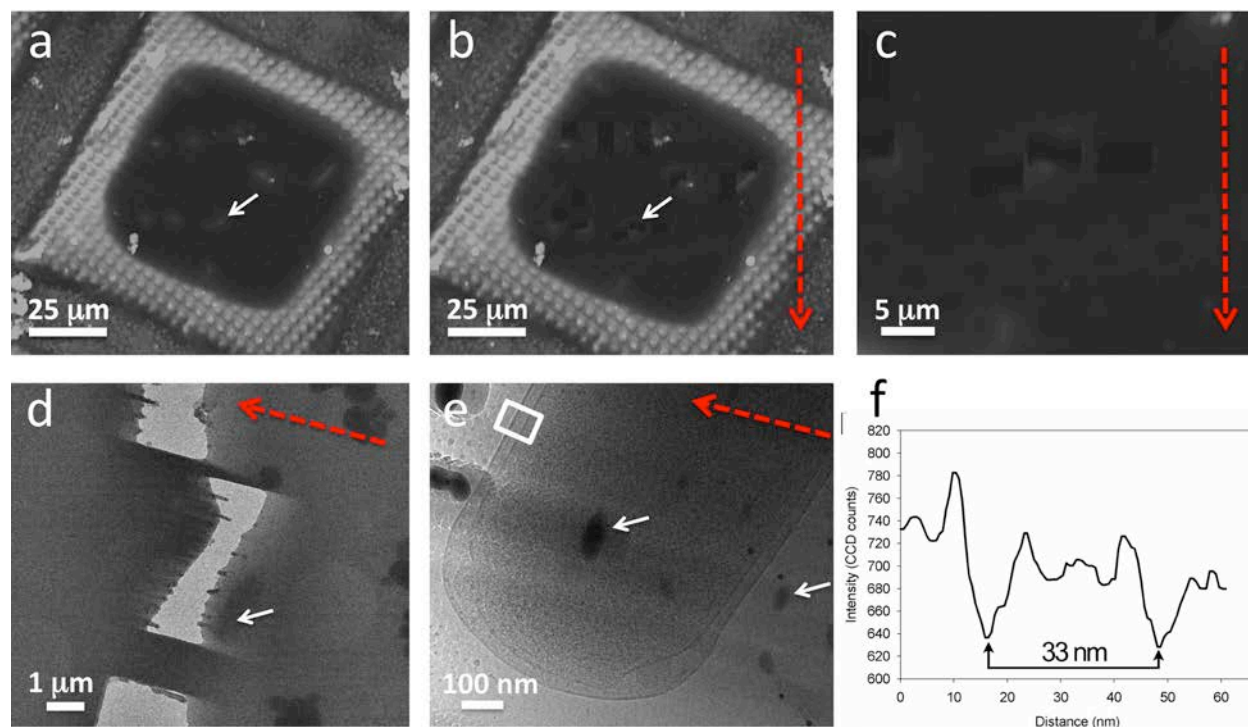


**Figure 26: Cryo FIB milling of E. Coli samples. (a) Unmilled SEM micrograph, the white arrow indicates the area of interest. (b) Milled SEM micrograph taken at medium magnification. (c) High magnification image of the area shown in (b). (d) Medium magnification, low dose, TEM projection image of the same area shown in (c). (e) High magnification, low dose, TEM projection image of the area indicated in (d) by the white arrow. (f) A density profile of the bacterial envelope scanned from the outer membrane (rectangular box in (e)) reveals the inner and outer membranes of the E. coli cell separated by ~33nm. The red arrows indicate milling direction.**

The low dose projection image of the selected E. coli cell (figure 26(e)) indicates a successful thinning process with little specimen damage or ice contamination. The cell membranes are well preserved with recognizable bilayer structures in the outer and inner

membranes (figure 26(e and f)). The reconstructed tomographic volume clearly shows that the top half of a single bacterium was trimmed away cleanly, leaving about 360 nm thick bottom half of the cell, as measured in the 3D volume (figure 27(g and h)). The tomogram exhibits no obvious structural damage or loss of detail in the uppermost slices of the remaining bacterium (figure 27(g and h)). The fine detailed 3D structure suggests that the effect of implanted Ga<sup>+</sup> ions on the frozen bacterial cell is negligible, confirming early simulation results [49]. The tomogram also reveals numerous structural features, in particular, putative ribosome molecules (figure 27(a), arrowhead) and membrane invaginations (figure 27(a and c)). The cytoplasmic membrane forms a continuous contour that curves into both periplasmic and cytoplasmic spaces (figure 27(a and c) black arrows), representing a new structural feature that has not been reported previously [46], [50], [51].

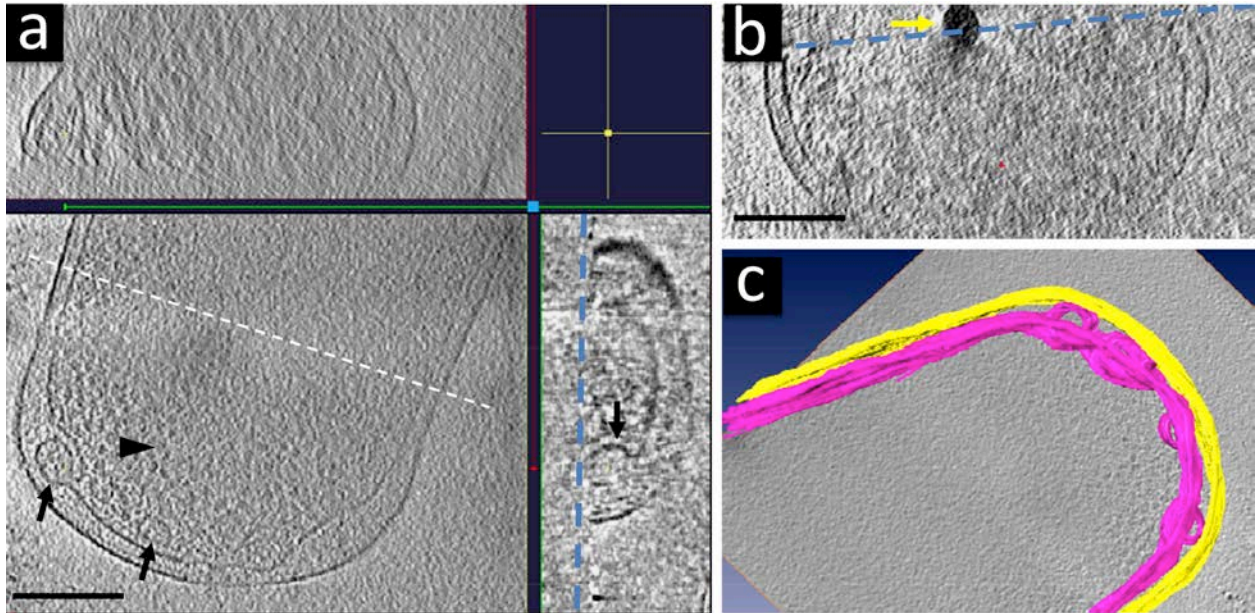


**Figure 27: Tomographic reconstruction of a FIB-milled *E. coli* cell. (a) Three orthogonal slices (0.62nm thick) from the tomogram at the cell pole are shown with small membrane invaginations (arrows) and putative ribosomes (arrowheads). A cross-section along the white dashed line indicated in (a) is shown in (b). FIB milling surface is indicated by a blue dashed line. (c) Surface-rendered model of *E. coli* envelope displaying membrane invaginations into both the cytoplasmic and periplasmic spaces.**

#### **4.2.4 HeLa**

Building upon our knowledge gained from the cryo-FIB milling of bacterial cells, we set out to process HeLa cells for cryo-ET analysis of their internal structures. There are several challenges in working with large and thick cells, as recognized previously [45], and, so far, no 3D structures from mammalian cells have been obtained using cryo-FIB approaches [45], [46]. The main challenge is the removal of sizeable volumes with a very low beam current (10 pA), required to

best preserve the structure but at the expense of increased milling time, which can take hours. We tested different milling conditions and optimized milling strategies for HeLa cells to acquire thin cellular wedges suitable for cryo-ET analysis. Using a 30 keV, 30 pA ion beam current at a 10° milling angle, a 5 x 10 μm wedge-shaped intracellular area (~20 μm from the edge of the cell) with a ~5 x 3 μm transparent region (figure 28(a-c)) was made in 30 minutes. The samples still exhibited some milling artifacts (figure 28(d), black arrows), however, they are not as prevalent as they are in some of the E. coli samples. We can observe in these samples in the 2D high magnification projection images many of the cell features, such as vesicles (figure 28(d), blue arrow) and mitochondria (figure 28(d), white arrow).

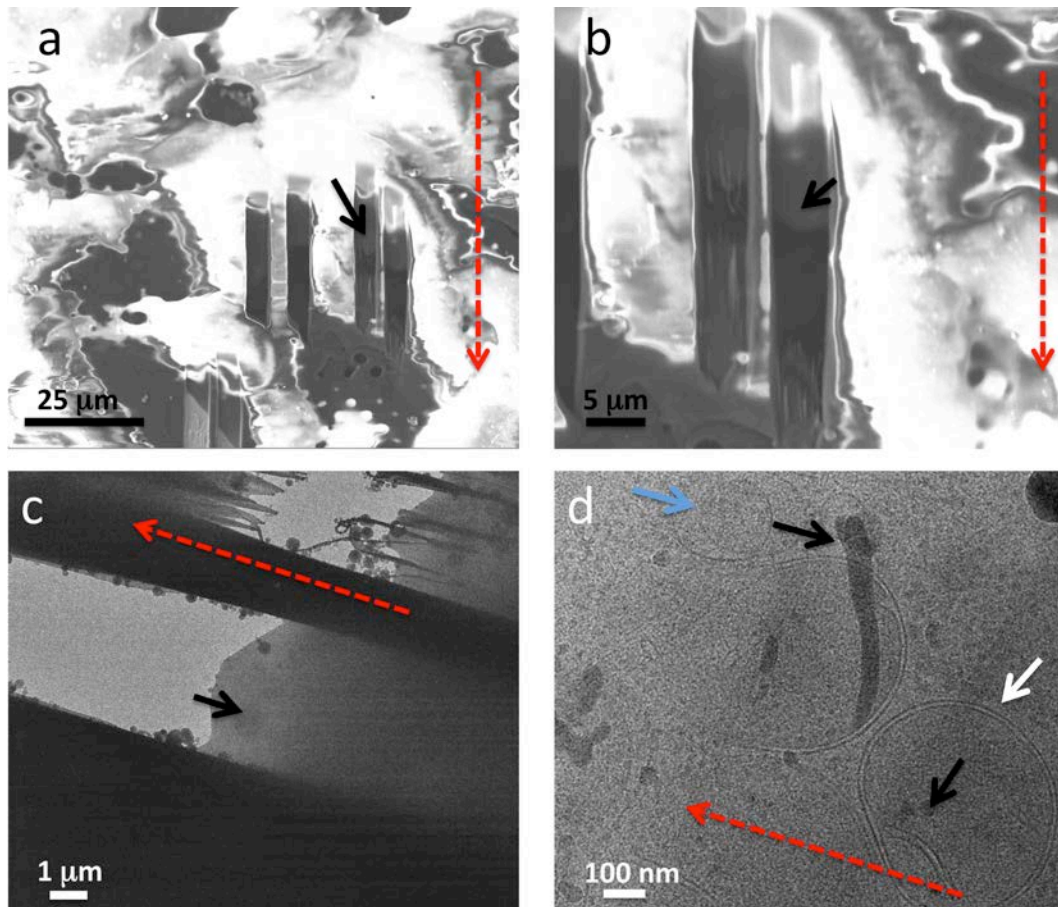


**Figure 28: HeLa cell milling. (a) Medium magnification SEM micrograph of a milling area. The black arrow indicates the mill of interest. (b) High magnification SEM micrograph of a mill. (c) Medium magnification, low dose TEM projection image of the area noted in (b) by the black arrow. (d) High magnification, low dose, TEM projection image of the area noted in (c) by the black arrow showing cell features, such as vesicles (blue arrow) and mitochondria (white arrow), as well as some artifacts (black arrows). The red arrows indicate milling direction.**

The 3D tomograms recorded from the milled region show high quality cellular ultrastructure with great detail (figure 29(a and b)). The thickness of this region, measured from the tomogram, is ~200 nm. Several structural features are clearly visible, including well-resolved mitochondrial membranes and cristae (Figure 29(a), black arrows), vesicles, actin filaments (figure 29(a), white arrow), and many individual protein complexes (figure 29(a), circles). The

cross-section of the 3D volume (figure 29(a)) clearly shows that half of the mitochondria were cleanly cut off without any noticeable damage on the very top of the milling surface. Overall, there was little frost contamination (figure 28, figure 26), suggesting that the samples were very well protected by the shutter mechanism in the cryo-FIB shuttle during transfer. Similar to the processing of *E. coli* cells, some milled material was deposited onto the freshly milled surface of the HeLa cell (figure 29(a), yellow arrows).

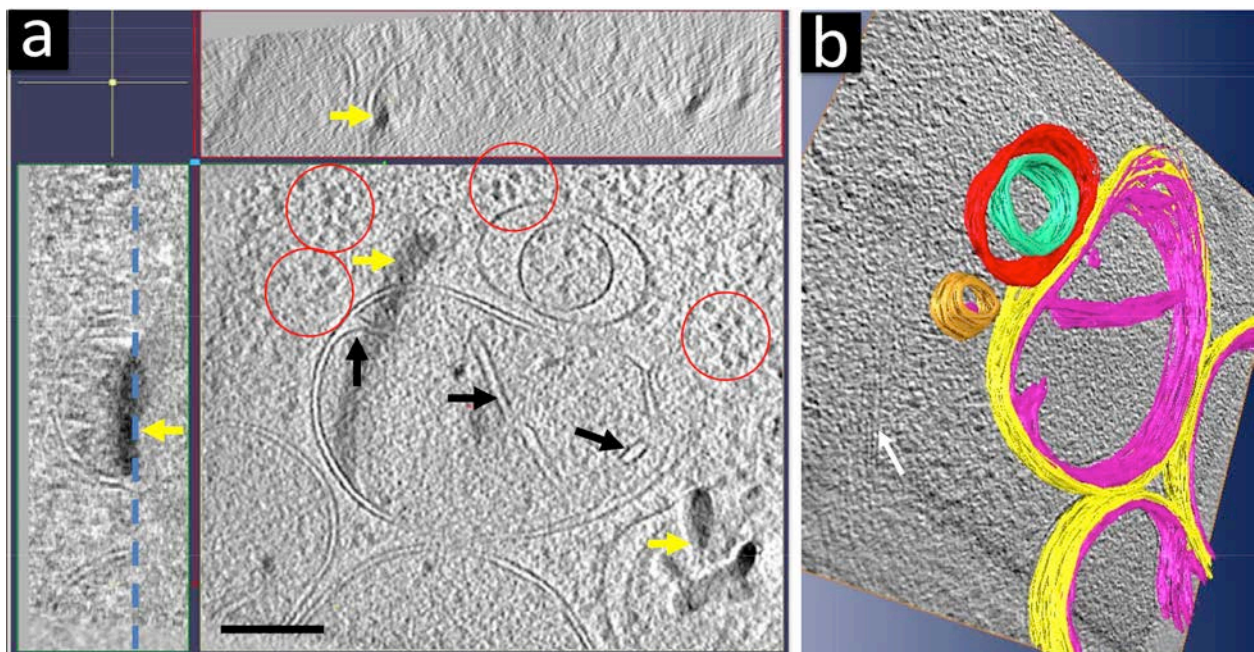


**Figure 29: Tomographic reconstruction of a FIB-milled HeLa cell. (a) Three orthogonal slices (0.62nm thick) from the tomogram are shown with clear mitochondrial membranes and cristae (black arrows). The milled surface is indicated by a blue dashed line. (b) Surface-rendered model of mitochondrial membranes and vesicles in a HeLa cell. Protein complex particles (red circles in (a)) and actin filaments (white arrow in (b)) are clearly visible. Yellow arrows indicate contamination.**

An additional challenge associated with milling of large cells is that, unlike the bacterial cells, frozen-hydrated HeLa cells are difficult to distinguish from the ice background in SEM

images, thus, identifying an area of interest is not easy. In figure 30, a comparison of *E. coli* cell and HeLa cells is shown. It can be seen that the *E. coli* (figure 30(a)) cells are easily distinguishable from the surrounding ice. The HeLa cells (figure 30(b)) are not as easily distinguishable and lack definition.

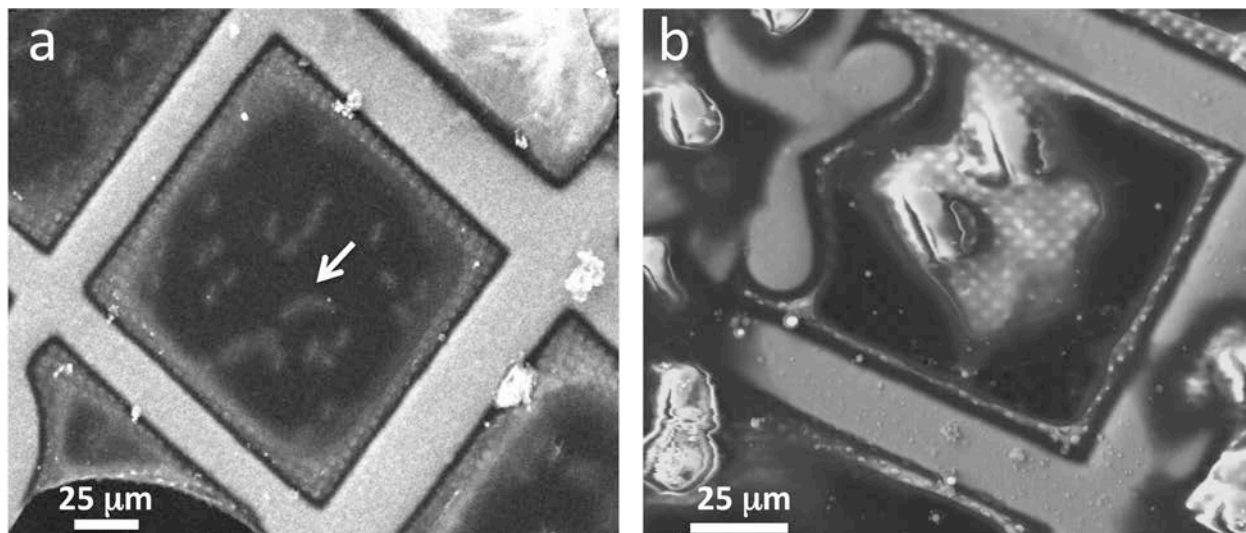


**Figure 30: Comparison of *E. coli* and HeLa cell grid squares. (a) *E. coli* grid square with an *E. coli* cell indicated with a white arrow. The cells have definition and can clearly be distinguished from the surrounding ice. (b) HeLa cell grid square. The cells lack definition and the exact outline of the cells are not easily discernable.**

To combat this problem, we used an approach developed in a previous correlative study [52] for selection of the target milling area. HeLa cells were cultured on EM finder grids and optical images of these were first recorded before plunge-freezing. Guided by the light microscopy images (figure 31), suitable HeLa cells were then identified and target regions were selected for subsequent cryo-FIB processing. With this approach, the rate for successful milling was greatly increased. More sophisticated correlative approaches by combining fluorescent light

microscopy and cryo-ET developed [45], [52–54] will further allow targeted molecular imaging, such as HIV-1 particles inside a host cell.

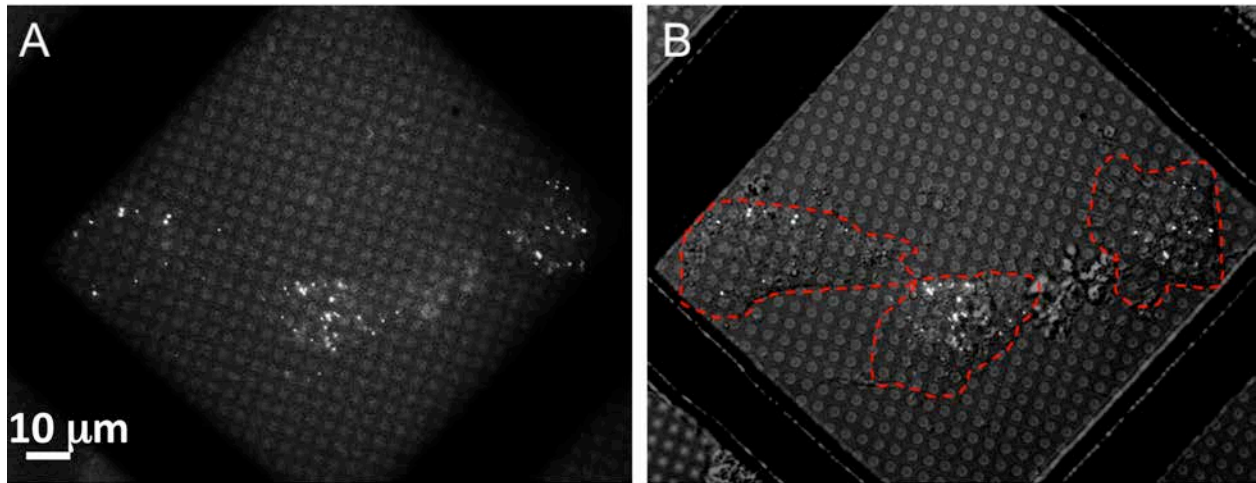


**Figure 31: Overview DIC images of HeLa cells cultured on a Quantifoil gold index grid. (A) GFP fluorescence image of HeLa cells infected with HIV-1 virus-like particles containing GFP-Vpr, recorded after 2 hours of infection with a 60x objective. (B) Differential interference contrast (DIC) image overlaid with the GFP signals. The cells are outlined with red dash lines.**

## **5.0 CONCLUSIONS**

### **5.1 FIB SLICE AND VIEW**

Our first experiments into the use of the FIB to produce a slice and view sample were not successful. The samples had too many artifacts present to make a successful computer reconstruction possible. In order to create more viable specimens, a thicker deposition layer was used, however this increased the time required and did not remove all of the milling artifacts. Also, in cryogenically frozen samples, these artifacts would be increased [8]. The time involved in creating even the unusable specimens was much too high to make this method viable for our research. We then decided to move the focus of our research to different cryo-FIB milling methods for other types of 3D reconstruction, specifically, cryo-ET.

### **5.2 CRYO-FIB MILLING**

The main limitations in cryo-ET applications arise from difficulties in preparing suitably thin, vitreous biological specimens. Cryo-FIB milling is a viable tool for thinning vitreous samples that can then be used for 3D tomographic structural analysis. This approach is a significant improvement over vitreous sectioning, especially due to the absence of mechanical artifacts [46]. We have designed and fabricated a cryo-shuttle, which directly accepts cryo-EM

specimen cartridges to streamline sample processing and 3D data collection and to allow very shallow FIB-milling angles and wider angular coverage for cryo-ET. We have successfully applied our cryo-shuttle to analysis of both bacterial cells and large mammalian cells, with good results. The reconstructed 3D volumes of FIB-thinned cells offer fine structural details of cultured HeLa cells for the first time. Our results show no mechanical stress and minimum specimen damage at the milling surfaces of processed cells.

## 6.0 FUTURE WORK

A few issues remain with the developed technique: Sample surface contamination, due to deposition of removed material, is often observed, especially when working with thick and large cells. Low beam (1 pA) polishing of freshly milled surfaces may help to clean up the deposited material. An improvement of the cryo-box/anti-contaminator in FIB/SEM chamber could further reduce the contamination. We also observed non-uniform streak-like patterns on the milling surface, as described previously [45], which may result from uneven surface topology of the target region. Because the gold beads were removed during milling of cell lamella, acquiring a 3D data set by cryo-ET becomes challenging. Future inclusion of intracellular fiducial markers, such as expression of ferritin [55] or metallothionein [56] molecules, will be helpful for carrying out 3D tomographic analyses. In addition, when working with HeLa cells, it was not easy to localize the cell and a particular cellular region of interest in SEM images. We correlated the SEM images with optical images of cells recorded before plunge-freezing to expedite searching and targeting appropriate milling sites. A more precise correlation can be achieved using a cryo-correlative light microscopy approach [52–54] for accurate localization of small targets. Our cryo-FIB shuttle design works seamlessly with the cryo-correlative light microscopy approach that developed previously [52], since both use the same specimen cartridge for handling the cryo-EM grids, thus making the system even more reliable, precise, robust and convenient to use with a high success rate. We anticipate that the combination of our cryo-FIB milling approach

with the correlative live-cell and cryo-ET method [52] will offer new ways to investigate virus and host cell interactions at many different stages of infection, as well as a variety of dynamic cell signaling events and other cellular processes.

The current method we are using to thin samples for cryo-ET only allows for viewing of the bottom slice of the sample. By creating “freely suspended lamella”, we can view different sections of the samples. The shuttle that we created for milling is already built to help with this procedure. The cartridge face can be reversed to allow milling from both surfaces of the sample in opposite directions. With this feature, a thin sample slab can be created either by two parallel mills from the same sample surface at a shallow angle (black arrows in figure 32 or by two anti-parallel mills from opposite surfaces (black and red arrows in figure 32).

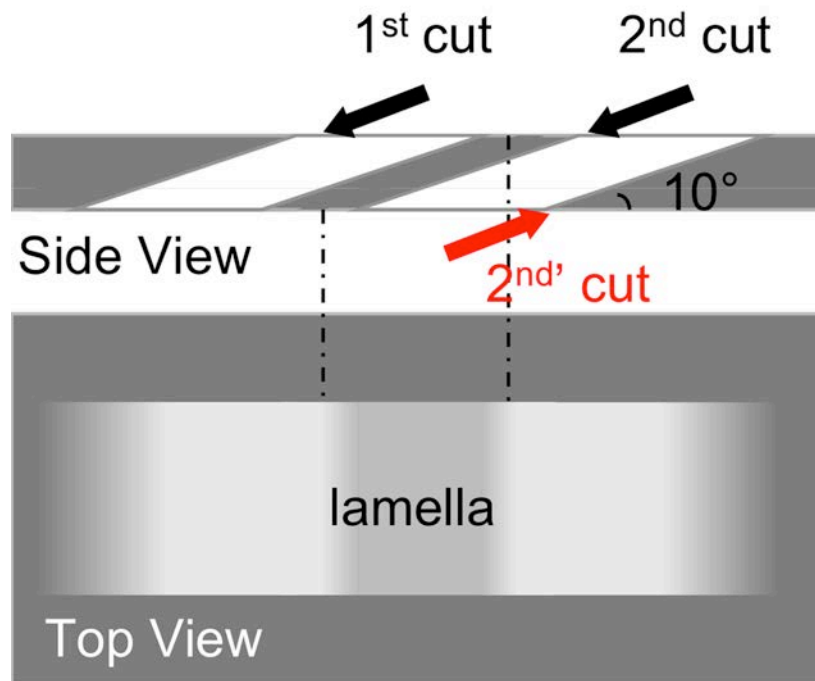


**Figure 32: Schematics of two FIB-milling strategies for producing vitrified cell lamella without “lift-out”: parallel milling (1<sup>st</sup> and 2<sup>nd</sup> cuts are in the same milling direction, black arrows) and anti-parallel milling (1<sup>st</sup> and 2<sup>nd</sup> cuts are in opposite milling directions on opposite surfaces, black and red arrows).**

The future direction of this research will be to focus on imaging other thick cells and biological samples that have not yet been imaged completely in the TEM. Since we have shown that large samples can be relatively easily thinned with few artifacts, we open up a large part of biology that has yet to be studied. Interactions between viruses and cells that are not currently understood can also be studied because now we can image further into the interior of the cell.

## **6.1 MATERIALS SCIENCE APPLICATIONS**

The same principles used for this research can be applied to materials science research. Using a FIB to create TEM samples is not a new application, and creating TEM cross sections is the preferred method for creating TEM samples in the FIB. However, soft materials, like polymers, or other membrane materials cannot be subjected to this process because they are too susceptible to damage, or are not strong enough to withstand the beam or other forces required for a successful TEM cross section. The methods we created could be applied to these soft materials in order to view them in the TEM.

By attaching the materials to a TEM stub, it would be possible to thin the samples at a glancing angle using low currents similar to the way that we thinned the biological specimens. This technique would allow for a targeted creation of TEM samples using the FIB without the need for the complex process involved in creating a TEM cross section (extensive milling, lift-out and reattaching the sample to the TEM grid). Also, using the proposed freely suspended lamella technique, any part of the sample could be thinned and viewed in the TEM, allowing for TEM characterization of materials not previously viewed in the TEM.

## REFERENCES

- [1] H. Fernandez-Moran, "Low-temperature preparation techniques for electron microscopy of biological specimens based on rapid freezing with liquid helium II," *Ann. N. Y. Acad. Sci.*, vol. 85, pp. 689-713, Apr. 1960.
- [2] J. Dubochet, M. Adrian, J. Lepault, and A. W. McDowell, "Emerging techniques: Cryo-electron microscopy of vitrified biological specimens," *Trends in Biochemical Sciences*, vol. 10, no. 4, pp. 143-146, Apr. 1985.
- [3] J. Dubochet, J.-J. Chang, R. Freeman, J. Lepault, and A. W. McDowell, "Frozen aqueous suspensions," *Ultramicroscopy*, vol. 10, no. 1-2, pp. 55-61, 1982.
- [4] D. Drobne, M. Milani, A. Zrimec, M. B. Zrimec, F. Tatti, and K. Drašlar, "Focused ion beam/scanning electron microscopy studies of Porcellio scaber (Isopoda, Crustacea) digestive gland epithelium cells," *Scanning*, vol. 27, no. 1, pp. 30-34, Jan. 2005.
- [5] L. H. P. Hekking, M. N. Lebbink, D. A. M. De Winter, C. T. W. M. Schneijdenberg, C. M. Brand, B. M. Humbel, A. J. Verkleij, and J. A. Post, "Focused ion beam-scanning electron microscope: exploring large volumes of atherosclerotic tissue," *J Microsc*, vol. 235, no. 3, pp. 336-347, Sep. 2009.
- [6] A. E. Bennett, K. Narayan, D. Shi, L. M. Hartnell, K. Gousset, H. He, B. C. Lowekamp, T. S. Yoo, D. Bliss, E. O. Freed, and S. Subramaniam, "Ion-abrasion scanning electron microscopy reveals surface-connected tubular conduits in HIV-infected macrophages," *PLoS Pathog.*, vol. 5, no. 9, p. e1000591, Sep. 2009.
- [7] M. F. Hayles, D. J. Stokes, D. Phifer, and K. C. Findlay, "A technique for improved focused ion beam milling of cryo-prepared life science specimens," *J Microsc*, vol. 226, no. Pt 3, pp. 263-269, Jun. 2007.
- [8] J. A. W. Heymann, M. Hayles, I. Gestmann, L. A. Giannuzzi, B. Lich, and S. Subramaniam, "Site-specific 3D imaging of cells and tissues with a dual beam microscope," *J Struct Biol*, vol. 155, no. 1, pp. 63-73, Jul. 2006.
- [9] K. Grünewald, O. Medalia, A. Gross, A. C. Steven, and W. Baumeister, "Prospects of electron cryotomography to visualize macromolecular complexes inside cellular

- compartments: implications of crowding,” *Biophysical Chemistry*, vol. 100, no. 1–3, pp. 577-591, Jan. 2003.
- [10] J. Kurner, Frangakis, A. S., and W. Baumeister, “Cryo-Electron Tomography Reveals the Cytoskeletal Structure of *Spiroplasma melliferum*,” *Science*, vol. 307, pp. 436-438, Jan. 2005.
- [11] G. E. Murphy, J. R. Leadbetter, and G. J. Jensen, “In situ structure of the complete *Treponema primitia* flagellar motor,” *Nature*, vol. 442, no. 7106, pp. 1062-1064, 2006.
- [12] O. Medalia, Weber, I., Frangakis, A. S., D. Nicastro, Gerisch, G., and W. Baumeister, “Macromolecular Architecture in Eukaryotic Cells Visualized by Cryoelectron Tomography,” *Science*, vol. 298, pp. 1209-1213, Nov. 2002.
- [13] M. Cyrklaff, A. Linaroudis, M. Boicu, P. Chlanda, W. Baumeister, G. Griffiths, and J. Krijnse-Locker, “Whole Cell Cryo-Electron Tomography Reveals Distinct Disassembly Intermediates of Vaccinia Virus,” *PLoS ONE*, vol. 2, no. 5, p. e420, 2007.
- [14] P. Zhang, E. Bos, J. Heymann, H. Gnaegi, M. Kessel, P. J. Peters, and S. Subramaniam, “Direct visualization of receptor arrays in frozen-hydrated sections and plunge-frozen specimens of *E. coli* engineered to overproduce the chemotaxis receptor Tsr,” *J Microsc*, vol. 216, no. Pt 1, pp. 76-83, Oct. 2004.
- [15] U. E. Maurer, B. Sodeik, and K. Grünewald, “Native 3D intermediates of membrane fusion in herpes simplex virus 1 entry,” *Proceedings of the National Academy of Sciences*, vol. 105, no. 30, pp. 10559 -10564, Jul. 2008.
- [16] I. Patla, T. Volberg, N. Elad, V. Hirschfeld-Warneken, C. Grashoff, R. Fassler, J. P. Spatz, B. Geiger, and O. Medalia, “Dissecting the molecular architecture of integrin adhesion sites by cryo-electron tomography,” *Nat Cell Biol*, vol. 12, no. 9, pp. 909 -915, 2010.
- [17] W. Baumeister, “From proteomic inventory to architecture,” *FEBS Letters*, vol. 579, no. 4, pp. 933-937, Feb. 2005.
- [18] A. Leis, B. Rockel, L. Andrees, and W. Baumeister, “Visualizing cells at the nanoscale,” *Trends Biochem. Sci.*, vol. 34, no. 2, pp. 60-70, Feb. 2009.
- [19] K. Grünewald, P. Desai, D. C. Winkler, J. B. Heymann, D. M. Belnap, W. Baumeister, and A. C. Steven, “Three-Dimensional Structure of Herpes Simplex Virus from Cryo-Electron Tomography,” *Science*, vol. 302, no. 5649, pp. 1396 -1398, Nov. 2003.
- [20] J. Liu, A. Bartesaghi, M. J. Borgnia, G. Sapiro, and S. Subramaniam, “Molecular architecture of native HIV-1 gp120 trimers,” *Nature*, vol. 455, no. 7209, pp. 109-113, Sep. 2008.

- [21] M. Bárcena, G. T. Oostergetel, W. Bartelink, F. G. A. Faas, A. Verkleij, P. J. M. Rottier, A. J. Koster, and B. J. Bosch, "Cryo-electron tomography of mouse hepatitis virus: Insights into the structure of the coronavirion," *Proceedings of the National Academy of Sciences*, Jan. 2009.
- [22] A. de Marco, B. Müller, B. Glass, J. D. Riches, H.-G. Kräusslich, and J. A. G. Briggs, "Structural Analysis of HIV-1 Maturation Using Cryo-Electron Tomography," *PLoS Pathog*, vol. 6, no. 11, p. e1001215, Nov. 2010.
- [23] C. M. Khursigara, X. Wu, P. Zhang, J. Lefman, and S. Subramaniam, "Role of HAMP domains in chemotaxis signaling by bacterial chemoreceptors," *Proc. Natl. Acad. Sci. U.S.A.*, vol. 105, no. 43, pp. 16555-16560, Oct. 2008.
- [24] A. Briegel, D. R. Ortega, E. I. Tocheva, K. Wuichet, Z. Li, S. Chen, A. Müller, C. V. Iancu, G. E. Murphy, M. J. Dobro, I. B. Zhulin, and G. J. Jensen, "Universal architecture of bacterial chemoreceptor arrays," *Proceedings of the National Academy of Sciences*, 2009.
- [25] L.-A. Carlson, A. de Marco, H. Oberwinkler, A. Habermann, J. A. G. Briggs, H.-G. Kräusslich, and K. Grünewald, "Cryo Electron Tomography of Native HIV-1 Budding Sites," *PLoS Pathog*, vol. 6, no. 11, p. e1001173, Nov. 2010.
- [26] W. Baumeister, "Electron tomography: towards visualizing the molecular organization of the cytoplasm," *Curr. Opin. Struct. Biol.*, vol. 12, no. 5, pp. 679-684, Oct. 2002.
- [27] D. F. Parsons, I. Uydees, and V. R. Matricardi, "High voltage electron microscopy of wet whole cells. Effect of different wet cell preparation methods on visibility of structures," *J Microsc*, vol. 100, no. 2, pp. 153-167, Mar. 1974.
- [28] D. F. Parsons, V. R. Matricardi, J. Subject, I. Uydess, and G. Wray, "High-voltage electron microscopy of wet whole cancer and normal cells: Visualization of cytoplasmic structures and surface projections," *Biochimica et Biophysica Acta (BBA) - Biomembranes*, vol. 290, pp. 110-124, Dec. 1972.
- [29] A. M. Glauert, "The high voltage electron microscope in biology," *J. Cell Biol.*, vol. 63, no. 3, pp. 717-748, Dec. 1974.
- [30] M. Adrian, J. Dubochet, J. Lepault, and A. W. McDowell, "Cryo-electron microscopy of viruses," *Nature*, vol. 308, no. 5954, pp. 32-36, Mar. 1984.
- [31] J. Frank, "Single-particle imaging of macromolecules by cryo-electron microscopy," *Annu Rev Biophys Biomol Struct*, vol. 31, pp. 303-319, 2002.
- [32] D. J. De Rosier and A. Klug, "Reconstruction of Three Dimensional Structures from Electron Micrographs," *Nature*, vol. 217, no. 5124, pp. 130-134, Jan. 1968.

- [33] B. F. McEwen and M. Marko, "The Emergence of Electron Tomography as an Important Tool for Investigating Cellular Ultrastructure," *Journal of Histochemistry & Cytochemistry*, vol. 49, no. 5, pp. 553 -563, May 2001.
- [34] J. W. Zhong, "3D Analysis on Via and Contact by Using Tomography," 2006.
- [35] R. McIntosh, D. Nicastro, and D. Mastronarde, "New views of cells in 3D: an introduction to electron tomography," *Trends in Cell Biology*, vol. 15, no. 1, pp. 43 -51, Jan. 2005.
- [36] D. J. DeRosier and P. B. Moore, "Reconstruction of three-dimensional images from electron micrographs of structures with helical symmetry," *Journal of Molecular Biology*, vol. 52, no. 2, pp. 355-369, Sep. 1970.
- [37] A. Steven and D. Belnap, "Electron Microscopy and Image Processing: An Essential Tool for Structural Analysis of Macromolecules," in *Current Protocols in Protein Science*, J. E. Coligan, B. M. Dunn, D. W. Speicher, and P. T. Wingfield, Eds. Hoboken, NJ, USA: John Wiley & Sons, Inc., 2005.
- [38] J. R. McIntosh, "Electron Microscopy of Cells," *The Journal of Cell Biology*, vol. 153, no. 6, p. F25 -F32, Jun. 2001.
- [39] A. Al-Amoudi, J. Dubochet, H. Gnaegi, W. Lüthi, and D. Studer, "An oscillating cryo-knife reduces cutting-induced deformation of vitreous ultrathin sections," *J Microsc*, vol. 212, no. Pt 1, pp. 26-33, Oct. 2003.
- [40] S. Shi, S. Sun, S. B. Andrews, and R. D. Leapman, "Thickness measurement of hydrated and dehydrated cryosections by EELS," *Microsc. Res. Tech.*, vol. 33, no. 3, pp. 241 -250, Feb. 1996.
- [41] P. Zhang and J. E. Hinshaw, "Three-dimensional reconstruction of dynamin in the constricted state," *Nat Cell Biol*, vol. 3, no. 10, pp. 922-926, Oct. 2001.
- [42] C.-E. Hsieh, M. Marko, J. Frank, and C. A. Mannella, "Electron tomographic analysis of frozen-hydrated tissue sections," *Journal of Structural Biology*, vol. 138, no. 1-2, pp. 63-73.
- [43] A. Al-Amoudi, D. Studer, and J. Dubochet, "Cutting artefacts and cutting process in vitreous sections for cryo-electron microscopy," *Journal of Structural Biology*, vol. 150, no. 1, pp. 109-121, Apr. 2005.
- [44] M. Marko, C. Hsieh, W. Moberlychan, C. A. Mannella, and J. Frank, "Focused ion beam milling of vitreous water: prospects for an alternative to cryo-ultramicrotomy of frozen-hydrated biological samples," *J Microsc*, vol. 222, no. 1, pp. 42-47, Apr. 2006.

- [45] A. Rigort, F. J. B. Bäuerlein, A. Leis, M. Gruska, C. Hoffmann, T. Laugks, U. Böhm, M. Eibauer, H. Gnaegi, W. Baumeister, and J. M. Plitzko, "Micromachining tools and correlative approaches for cellular cryo-electron tomography," *J. Struct. Biol.*, vol. 172, no. 2, pp. 169-179, Nov. 2010.
- [46] M. Marko, C. Hsieh, R. Schalek, J. Frank, and C. Mannella, "Focused-ion-beam thinning of frozen-hydrated biological specimens for cryo-electron microscopy," *Nat Meth*, vol. 4, no. 3, pp. 215-217, Mar. 2007.
- [47] M. Nastasi, J. Mayer, and J. K. Hirvonen, *Ion-Solid Interactions: Fundamentals and Applications*. Cambridge University Press, 1996.
- [48] J. R. Kremer, D. N. Mastronarde, and J. R. McIntosh, "Computer visualization of three-dimensional image data using IMOD," *J. Struct. Biol.*, vol. 116, no. 1, pp. 71-76, Feb. 1996.
- [49] Y. Yabuuchi, S. Tametou, T. Okano, S. Inazato, S. Sadayama, Y. Yamamoto, K. Iwasaki, and Y. Sugiyama, "A study of the damage on FIB-prepared TEM samples of Al<sub>x</sub>Ga<sub>1-x</sub>As," *J Electron Microsc (Tokyo)*, vol. 53, no. 5, pp. 471-477, 2004.
- [50] J. S. Dewey, C. G. Savva, R. L. White, S. Vitha, A. Holzenburg, and R. Young, "Micron-scale holes terminate the phage infection cycle," *Proc. Natl. Acad. Sci. U.S.A.*, vol. 107, no. 5, pp. 2219-2223, Feb. 2010.
- [51] A. Kishimoto-Okada, S. Murakami, Y. Ito, N. Horii, H. Furukawa, J. Takagi, and K. Iwasaki, "Comparison of the envelope architecture of E. coli using two methods: CEMOVIS and cryo-electron tomography," *J Electron Microsc (Tokyo)*, vol. 59, no. 5, pp. 419-426, 2010.
- [52] S. Jun, D. Ke, K. Debiec, G. Zhao, X. Meng, Z. Ambrose, G. A. Gibson, S. C. Watkins, and P. Zhang, "Direct visualization of HIV-1 with correlative live-cell microscopy and cryo-electron tomography," *Structure*, vol. 19, no. 11, pp. 1573-1581, Nov. 2011.
- [53] A. Sartori, R. Gatz, F. Beck, A. Rigort, W. Baumeister, and J. M. Plitzko, "Correlative microscopy: bridging the gap between fluorescence light microscopy and cryo-electron tomography," *J. Struct. Biol.*, vol. 160, no. 2, pp. 135-145, Nov. 2007.
- [54] J. M. Plitzko, A. Rigort, and A. Leis, "Correlative cryo-light microscopy and cryo-electron tomography: from cellular territories to molecular landscapes," *Curr. Opin. Biotechnol.*, vol. 20, no. 1, pp. 83-89, Feb. 2009.
- [55] Q. Wang, C. P. Mercogliano, and J. Löwe, "A Ferritin-Based Label for Cellular Electron Cryotomography," *Structure*, vol. 19, no. 2, pp. 147-154, Feb. 2011.
- [56] C. P. Mercogliano and D. J. DeRosier, "Concatenated Metallothionein as a Clonable Gold Label for Electron Microscopy," *J Struct Biol*, vol. 160, no. 1, pp. 70-82, Oct. 2007.